Selective high-temperature CO_2 electrolysis enabled by oxidized carbon intermediates

Theis L. Skafte[1,2,3,6], Zixuan Guan[4], Michael L. Machala[2], Chirranjeevi B. Gopal[2], Matteo Monti[2], Lev Martinez[1], Eugen Stamate[1], Simone Sanna[1], Jose A. Garrido Torres[3], Ethan J. Crumlin[5], Max García-Melchor[7], Michal Bajdich[3 *], William C. Chueh[2,8 *] and Christopher Graves[1,2,3 *]

[1]Department of Energy Conversion and Storage, Technical University of Denmark, Risø campus, Frederiksborgvej 399, 4000 Roskilde, Denmark.

[2]Department of Materials Science and Engineering, Stanford University, 496 Lomita Mall, Stanford, CA 94305, USA.

[3]SUNCAT Center for Interface Science and Catalysis, SLAC National Accelerator Laboratory, 2575 Sand Hill Road, Menlo Park, CA 94025, USA.

[4]Department of Applied Physics, Stanford University, 348 Via Pueblo Mall, Stanford, CA 94305, USA.

[5]Advanced Light Source, Lawrence Berkeley National Laboratory, 1 Cyclotron Road, Berkeley, CA 94720, USA.

[6]Haldor Topsoe A/S, Haldor Topsøes Allé 1, 2800 Kgs. Lyngby, Denmark.

[7]School of Chemistry, CRANN and AMBER Research Centres, Trinity College, College Green, Dublin 2, Ireland.

[8]Stanford Institute for Materials and Energy Sciences, SLAC National Accelerator Laboratory, 2575 Sand Hill Road, Menlo Park, CA 94025, USA.

*Correspondence to: cgra@dtu.dk, wchueh@stanford.edu, and bajdich@slac.stanford.edu

Abstract: High-temperature CO_2 electrolyzers offer exceptionally efficient storage of renewable electricity in the form of CO and other chemical fuels, but conventional electrodes catalyze destructive carbon deposition. Ceria catalysts are known carbon inhibitors for fuel cell (oxidation) reactions, however for the more severe electrolysis (reduction) conditions, catalyst design strategies remain unclear. Here we establish the inhibition mechanism on ceria and show selective CO_2 to CO conversion well beyond the thermodynamic carbon deposition threshold. Operando X-ray photoelectron spectroscopy during CO_2 electrolysis – using thin-film model electrodes consisting of samarium-doped ceria, nickel, and/or yttria-stabilized zirconia – together with density functional theory modeling reveal the crucial role of oxidized carbon intermediates in preventing carbon buildup. Using these insights, we demonstrate stable electrochemical CO_2 reduction with a scaled-up 16 cm^2 ceria-based solid oxide cell under conditions that rapidly destroy a nickel-based cell, leading to substantially improved device lifetime.

Main Text: CO_2 utilization is expected to play a key role in achieving a carbon-neutral sustainable energy economy. Electrochemical CO_2 reduction, in particular, is a promising way to store intermittent electricity derived from solar and wind in the form of chemicals, such as synthetic hydrocarbons compatible with the existing energy infrastructure, and is therefore an essential technology in decarbonization strategies [1–4]. Currently, the most efficient CO_2 electrolysis technology is the elevated-temperature solid oxide electrochemical cell (SOC), which utilizes O^{2-} as the mobile ion. SOCs produce CO and O_2 at the thermoneutral voltage of ~1.46 V with current densities exceeding 1 A/cm^2 – similar to steam electrolysis, which can be carried out simultaneously in the same cell to produce syngas or methane [1,2,5,6]. The same SOC can be operated in reverse as a fuel cell to re-oxidize the fuel products, thereby enabling operation as a flow battery [6,7]. Another important application is O_2 (and CO) production from the CO_2-rich atmosphere of Mars for rocket propulsion and life support, which will be demonstrated on the NASA Mars 2020 rover [8].

A key challenge for CO_2 electrolysis in SOCs is the competition between CO generation ($2CO_2(g) \rightarrow 2CO(g) + O_2(g)$) and C deposition ($CO_2(g) \rightarrow C + O_2(g)$) [8–10]. In technologically-relevant SOCs, Ni is the most commonly employed electrocatalyst in the fuel electrode (typically as a porous composite with yttria-stabilized zirconia, YSZ). Unfortunately, Ni is also an excellent catalyst for destructive carbon formation [11] during electrolysis, which eventually fractures the porous electrode [9,10,12]. The global thermodynamics of carbon formation are understood in terms of CO disproportionation, also known as the Boudouard reaction ($2CO(g) \rightleftharpoons C + CO_2(g)$), which is obtained by subtracting the two aforementioned reactions [8,9,13], see Supplementary Information. Boudouard deposition is also a concern in fuel cell mode, albeit with much less severity than in electrolysis due to the oxidizing environment [14,15]. Advanced carbon-tolerant fuel cell electrodes almost universally include $CeO_{2-\delta}$ (ceria, substituted with trivalent cations such as Sm and Gd), or other oxygen-storing oxides, as an active component [16–22]. It was recently proposed that carbon tolerance on ceria in fuel cells could also extend to electrolysis cells [10].

Rational design rules for these carbon-resistant electrode materials have been largely inferred from studies on carbon deposition during steam reforming in heterogeneous catalysis [15,23,24]. For example, density functional theory (DFT) calculations showed that adsorbed oxidized carbon species provide an inhibiting effect on the deposition of carbon on terraces and steps in heterogeneous catalysts [25,26], and it was suggested that increasing their formation rate will increase the carbon tolerance [15]. Participation of carbonate species in hydrocarbon oxidation in solid-oxide fuel cells was investigated using Raman spectroscopy, suggesting that carbonate oxidizes deposited carbon into adsorbed carbon groups [19]. Nevertheless, CO_2 electrolysis in SOCs is fundamentally distinct from these processes. For example, under high conversion conditions, $CO_2(g)$ and $CO(g)$ are present in significant concentrations, which directly affects the coverage of reaction intermediates on the electrode surface. Moreover, the surface oxygen activity is controlled by the electrode overpotential, again influencing the rates of CO(g) and C generation. Neither is the case in heterogeneous catalysis. For ceria-based electrodes, their observed carbon tolerance during CO_2

electrolysis is loosely attributed to the enhanced oxygen-storage capacity [10]. Recent work showed that surface oxygen vacancies are saturated with carbonates during CO_2 electrolysis [27], which participates in the reduction of CO_2(g) to CO(g) on ceria [27–29]. However, the connection to carbon deposition, and more importantly, strategies to inhibiting it, remains elusive.

In this work, combining dense thin-film electrodes, *operando* ambient-pressure X-ray photoelectron spectroscopy (APXPS) and DFT calculations, we show that surface oxygen vacancies on ceria control the relative stability of carbonate (CO_2* on O, hereafter denoted as CO_2*_O, where the subscript indicates the bonding site), carboxylate ($CO*_O$) and adsorbed carbon monoxide ($C*_O$) reaction intermediates during CO_2 electrolysis, and therefore the onset overpotential for carbon deposition. Specifically, on the oxygen-vacancy-rich ceria surface, both experiments and computations show that carbon atoms are energetically trapped as oxidized carbon species relative to solid carbon (but not excessively trapped relative to CO(g)), thus delaying carbon formation. We propose that abundant carbonates on ceria, which are absent on Ni-YSZ, could also react and remove transiently deposited carbon to produce $CO*_O$ in a surface reverse-Boudouard reaction. Thus, two general design rules emerge: 1) To kinetically prevent carbon deposition during CO_2 electrolysis, carbon atoms need to be energetically trapped as oxidized carbon intermediates such that CO_2(g) and CO(g) are not easily reduced to carbon. 2) Having a high carbonate coverage facilitates the reverse Boudouard reaction. Finally, we use these insights to engineer and demonstrate a scaled-up 16 cm^2 SOC with a porous ceria electrode, achieving stable and selective CO_2 electrolysis beyond the thermodynamic carbon deposition threshold.

Operando **X-ray photoelectron spectroscopy**

To elucidate the carbon deposition mechanism on Ni and the carbon tolerance of ceria-based electrodes, *operando* APXPS [27,28,30,31] was carried out on three types of thin-film electrodes at 550 °C, schematically shown in Fig. 1: YSZ(100) single crystals with A) dispersed Ni nanoparticles

and a microfabricated Ni patterned current collector ("Ni-YSZ"), B) a samarium-doped ceria thin-film electrode grown by pulsed-laser deposition (PLD) with dispersed Ni nanoparticles and a buried patterned current collector ("Ni-SDC"), and C) a Ni-free samarium-doped ceria thin-film electrode, also prepared by PLD and with a buried current collector ("SDC") [32]. These model electrodes represent the most common material sets employed in SOCs [7–10,14–17,22,33]. The counter electrode was nanoporous ceria/Pt for all samples. The gas atmosphere during APXPS measurements was chosen to avoid thermochemical Boudouard carbon deposition at open-circuit: 1:1 CO(g):CO_2(g) atmosphere with a total pressure of 480-500 mTorr for the Ni-SDC and Ni-YSZ electrodes, and 150 mTorr for the SDC electrode. At this temperature and pressure, the carbon deposition threshold is ~98% ±1% CO(g) balanced by CO_2(g) (uncertainty due to pressure range), much higher than the 50% CO(g) supply. Therefore, carbon deposition, if any, must be driven electrochemically by applying cathodic overpotential on the working electrode beyond the global thermodynamic threshold for carbon deposition, which corresponds to –120 ±72 mV overpotential (see Supplementary Information and Supplementary Fig. 1).

By gradually changing the overpotential from anodic to cathodic, we quantify the onset potential of carbon deposition for each electrode with APXPS, which is sensitive to the sub-monolayer of deposited carbon, and investigate the evolution of C- and O-containing species. As shown in Fig. 1g-i, carbon growth is indicated by the photoemission peak at ~285 eV. Quantified peak area as a function of overpotential is shown in Fig. 1j-l. For the Ni-YSZ electrode, adventitious carbon was present before biasing, as we did not flow oxygen prior to the experiment due to susceptibility of Ni to oxidation. Neither the carbon peak nor the lattice oxygen feature in O 1s photoemission peak (~530.5 eV at open-circuit for Ni-YSZ) changed significantly between +200 mV (anodic) to –100 mV (cathodic), just below the carbon deposition threshold. Upon reaching –150 mV overpotential, the intensity of the carbon peak grew considerably and continued to do so at larger overpotentials. This onset overpotential is close to the global thermodynamic threshold for carbon deposition, –120 ±72 mV. A concomitant decrease in the YSZ lattice oxygen peak from O

1s at –150 mV (Supplementary Fig. 2) further confirms carbon deposition, which covers the oxide surface. Based on these observations, we postulate that only adventitious carbon is present on the sample between +200 mV (anodic) to –100 mV (cathodic), while at –150 mV additional carbon is deposited on account of the overpotential. The ceria-containing electrodes required a significantly higher overpotential to observe the onset of carbon formation. For Ni-SDC, the threshold was between –250 mV and –300 mV; for SDC in the absence of Ni, even higher overpotential is required – between –300 mV and –600 mV, consistent with a previous observation that carbon can form on ceria with sufficiently high overpotential [34]. Notably, for all three electrodes, carbon can be partially removed by applying anodic overpotentials (Fig. 1g-i and Supplementary Fig. 3).

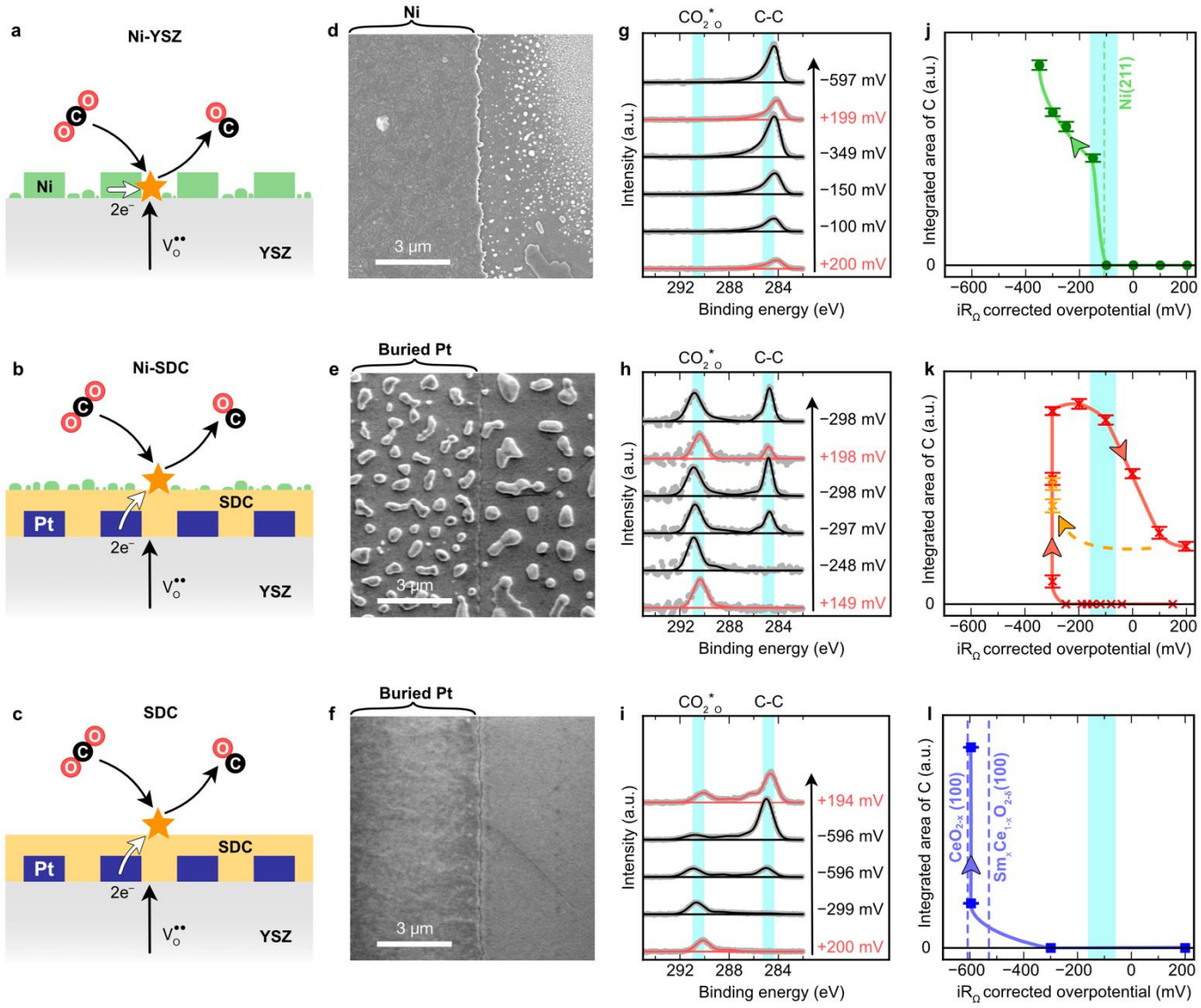

Fig. 1. Model electrodes employed and measurements of carbon formation/oxidation as the overpotential is varied. a-c, Illustrations of the Ni-YSZ, Ni-SDC, and SDC electrodes, with a buried Pt pattern for the SDC-containing electrodes. **d-f**, Planar SEM images of the surfaces and interfaces after testing. The Ni-YSZ electrode had <40 nm Ni particles next to the pattern. **g-i**, XPS spectra of C 1s with an inelastic mean free path of 0.6 nm showing the dependence of the carbon peak at ~285 eV on the applied overpotential (vs. $CO(g)/CO_2(g)/O^{2-}$, see Supplementary Information). The arrows indicate the chronological order of measurements. The binding energy of each spectrum at OCV are calibrated with the Au $4f_{7/2}$ peak (84.0 eV) from an Au foil Fermi coupled with the photoelectron analyzer. The gas phase peaks for CO and CO_2 have here been fitted and removed (Supplementary Fig. 4), and all spectra have been normalized to the maximum carbon intensity. **j-l**, Integrated areas of the XPS C-C (~285 eV) peaks. Lines are only meant to guide the eye. Fitting error (standard deviation) is indicated by error bars. Adventitious carbon present on the Ni-YSZ sample has been fitted and removed from **j**. The thermodynamic threshold for carbon

formation is shown by the cyan bars, accounting for experimental uncertainties and differences. The dotted lines indicate the DFT calculated onset overpotentials (see also Fig. 4).

As can be seen in the photoelectron spectra (Fig. 2a and also Fig. 1g-i), not only does the onset of carbon deposition vary dramatically between the three electrodes, but also the surface carbon chemistry. Across the electrode configurations and overpotentials examined, the C 1s spectra consist of asymmetric and/or multiple peaks, suggesting that a range of carbon-containing species form during electrolysis. See Supplemental Information for fitting procedures. For Ni-YSZ, the binding energy (BE) shows mixed sp^2 and sp^3 type carbon (Fig. 2a, 284.3 and 284.7 eV, respectively [35–37]). The presence of sp^2 carbon, in particular, suggests the growth of graphitic carbon or carbon nanotubes, which indeed was observed by post mortem scanning electron microscopy (SEM) (Fig. 2b). On the other hand, for Ni-SDC and SDC electrodes, the summit BE is found close to 284.7 eV and peak fitting indicates that Ni-SDC (and SDC) electrodes deposit mostly sp^3 carbon, i.e., amorphous or diamond-like carbon [38]. No carbon with discernable microstructure was detected with post mortem SEM, consistent with carbon being deposited as a thin, amorphous layer. We note that because these carbon species are electronically (Fermi) coupled to the photoelectron analyzer, their BEs do not change with overpotential (as confirmed in Supplementary Fig. 5), enabling a direct comparison to literature values. We also note that the quantification results are somewhat sensitive to the full-width half-maximum constraints applied. For completeness, we also investigated Ni carbide species through Ni 2*p* XPS for Ni-YSZ. The Ni $2p_{3/2}$ spectrum (Supplementary Fig. 6) resembles that of a pure metal [39]. Thus, we conclude that there are no carbides, at least near the Ni surface.

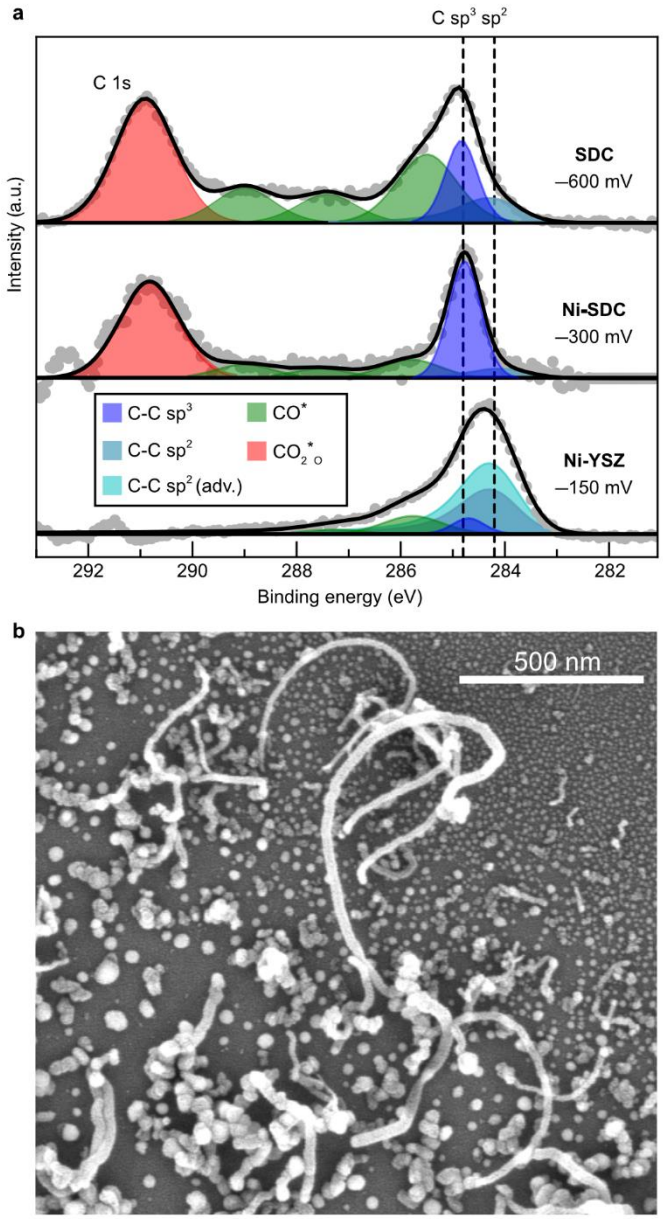

174

175 **Fig. 2. Surface carbon species observed with APXPS and SEM. a**, Fitting of XPS peaks for all
176 three electrodes at the electrode overpotential (rounded by 10 mV) where carbon was first
177 deposited. The gas phase peaks for CO and CO_2 have been fitted and removed (Supplementary Fig.
178 4), the background has been subtracted, and carbon peak intensity has been normalized. **b**, Planar
179 SEM of carbon nanotube growth on dispersed Ni nanoparticles next to the Ni pattern (Ni-YSZ
180 electrode). Scale bar is 500 nm.

181

182 The most pronounced spectroscopic difference between Ni-YSZ and the ceria-containing electrodes
183 is the presence of significant C 1s photoelectron intensities at BEs above that of the sp^2 and sp^3
184 carbon during CO_2 electrolysis, which correspond to various oxidized carbon species (Fig. 2a). The

fact that Ni-YSZ deposits carbon much more readily than Ni-SDC and SDC points to the importance of these oxidized carbon species. Specifically, on Ni-SDC and SDC electrodes, we observe significant amounts of carbonate (CO_2*$_O$) at all overpotentials (BE ~290.5 eV [27,31,40,41]) and various other oxygenated carbon species (CO*) such as C-O, C=O, and/or carboxylate (BE between ~ 286 and 290 eV, between the carbonate and carbon peaks [37,40–43]). As these peaks were not observed for Ni-YSZ and are qualitatively similar between Ni-SDC and SDC, we attribute them to species on ceria. It is noted that the BE shift of the CO_2*$_O$ peak with applied overpotential (Fig. 1h-i and Supplementary Fig. 5) is likely due to CO_2*$_O$ not being Fermi coupled with the photoelectron analyzer [31], although a difference in adsorbate charge cannot be excluded.

Fig. 3 illustrates the evolution of these oxidized carbon species as a function of overpotential. For the ceria electrodes, carbonate adsorbate is present in high concentrations at all studied conditions. With increasing cathodic (reductive) overpotential prior to the onset of carbon deposition, the carbonate coverage grew, consistent with lattice oxygen near an oxygen vacancy being the adsorption site [27]. At the onset of carbon deposition, the carbonate coverage decreased significantly, likely corresponding to the coverage of the ceria surface with carbon and blockage of carbonate adsorption sites.

Next, we turn to other oxidized carbon species. These are generally less oxidized than carbonates, which we collectively refer to as CO*, as quantitative peak assignment is challenging. Before the onset of carbon deposition, their coverage is significantly lower than that of carbonates, approaching the detection limit. Interestingly, at the onset of carbon deposition, the signal for CO* increased concomitantly with carbon while the carbonate concentration decreased. We briefly speculate on the mechanism. Upon the formation of CO* adsorbate (carboxylate), two pathways are possible: (1) chemical desorption as CO(g) and (2) further electrochemical deoxygenation to C. These can occur in parallel. Before the onset of carbon deposition at around –300 mV, the first pathway prevails. Between –250 and –300 mV, the current density increases by 44%, which is accompanied by a significant increase in both carboxylate and carbon coverage. Given the large

jump in C and CO* coverage over a small voltage window and the lack of large change in current density, we associate the coverage change with electrochemical pathway (2) rather than chemical pathway (1). We first consider the possibility that the increase in CO* could be associated with the driving force needed to deposit C (i.e., buildup of reactant). This is possible if carbon deposition was the only reaction. An alternative explanation is that the buildup of CO* is due to the decomposition of C via the surface reverse Boudouard reaction, $2CO_2{}^*{}_O + C\text{-}C + 2S_O \rightarrow 4CO^*{}_O$, with S_O denoting an adsorbate-free oxygen site. If such a reaction proceeds quickly enough, it could establish a higher CO* coverage concomitant with increase in C coverage. This reaction occurs over the ceria surface for SDC, and additionally across the ceria/Ni/gas triple-phase boundary for Ni-SDC. The rate of this reaction is likely enhanced by the high carbonate coverage, which is a reactant. We note other pathways are also possible.

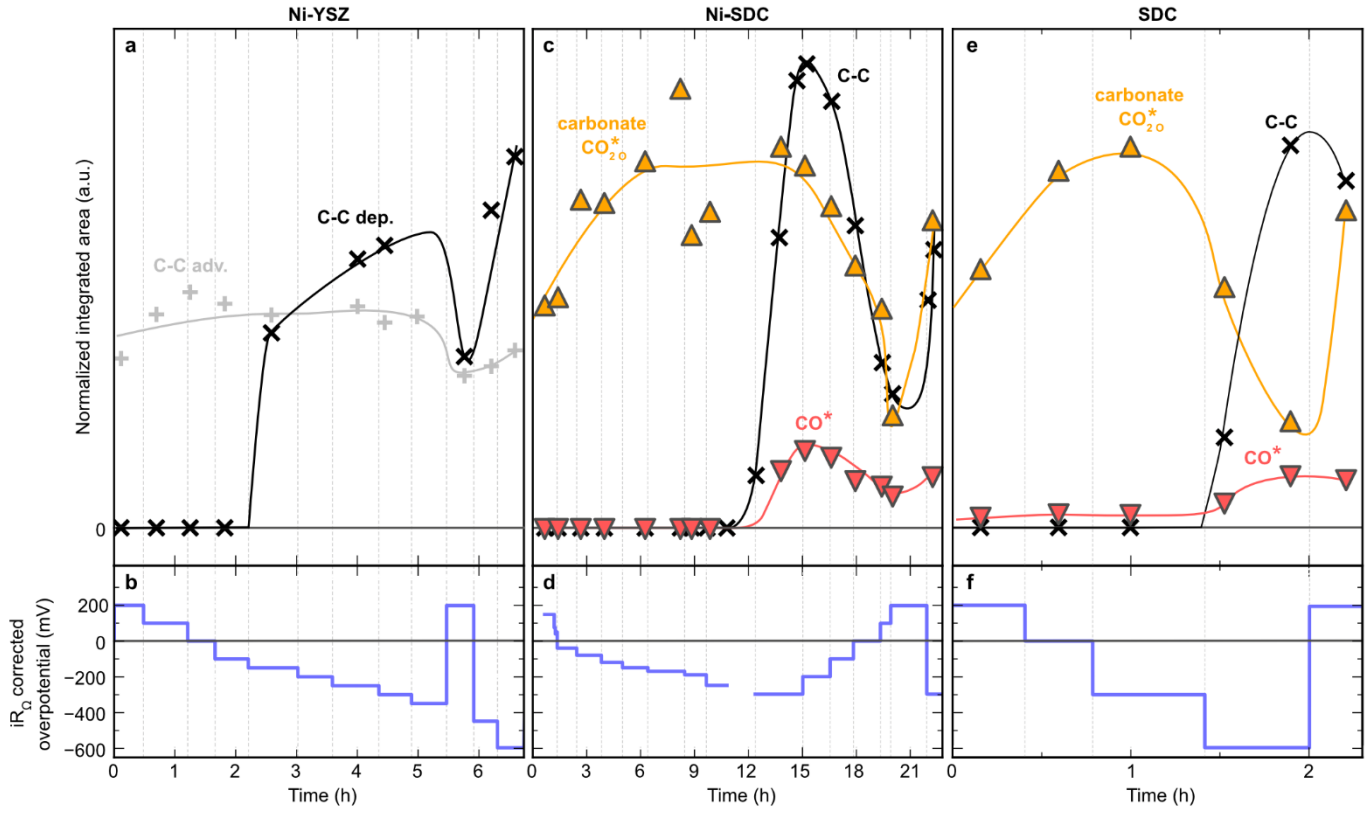

Fig. 3. Evolution of surface carbon species as overpotential is varied. a, **c** and **e**, Evolution of the normalized integrated areas of carbon, $CO_2{}^*{}_O$ and CO* from APXPS peaks with time for each electrode as the applied iR corrected overpotentials are varied, **b**, **d** and **f**. The integrated areas are averages of several measurements and were normalized to the CO_2(g) peak, which was normalized

to the absolute pressure. **a-b**, Ni-YSZ, **c-d**, Ni-SDC, and **e-f**, SDC. Lines are only meant to guide the eye. In **d**, voltage data was not recorded from ~11 to 12 h.

Density functional theory modeling

In order to shed light on the different behavior of the three electrodes, we modelled a series of (non)-stoichiometric ceria and Ni surfaces, and investigated the thermodynamics of various reaction intermediates by DFT. To use the same notation for Ni and ceria, we will now simplify the notation and omit the adsorption site as earlier indicated as subscript for CO_2*. We consider the adsorption of CO_2(g) and stepwise electrochemical deoxygenation, with each step being a two-electron process: $CO_{2(g)} \rightarrow CO_2^* \rightarrow CO^* + (O^{2-}{}_{YSZ} - 2e^-_{CC}) \rightarrow C^* + 2(O^{2-}{}_{YSZ} - 2e^-_{CC})$, where O^{2-} and e^- indicates the oxygen ions and electrons that migrate through the YSZ solid electrolyte and current collector (CC), respectively (Fig. 4). The overpotential is simulated via the Nernstian chemical potential of oxygen, $\Delta\mu O = \Delta\mu O^{2-}{}_{YSZ} - 2\Delta\mu e^-_{CC}$, where Δ indicates the difference with respect to open-circuit. The pathway starting with CO(g) is also implicitly calculated, but its chemical potential is fixed to CO_2(g) via $\Delta\mu O$ at zero energy. In the case of Ni, we do not explicitly simulate the three-phase boundary but rather include the electrochemical driving force via $\Delta\mu O$.

For ceria, we simulated bulk-truncated (111) stoichiometric CeO_2 and surface-only oxygen-deficient $CeO_{1.875}$ and $CeO_{1.75}$, as well as (100) and (110) surface-only oxygen-deficient $CeO_{1.875}$. Furthermore, we modelled a surface-only Sm-doped and oxygen-deficient $Sm_{0.25}Ce_{0.75}O_{1.875}$ (100), which is similar to the electrode characterized in the APXPS experiments (Fig. 4d). Given the YSZ substrate has a (100) termination, this is likely the termination of the SDC surface in our experiments, although we also considered (111) and (110) surfaces as these may coexist in the experiments. For oxygen-deficient ceria, which is experimentally relevant in the reducing atmosphere [27], DFT+U calculations reveal that (100) and (110) surfaces provide good anchoring sites for CO_2* adsorbates on oxygen, resulting in the formation of carbonate ($CO_2{}^*{}_O$) [44] with close to –2e charge (Supplementary Fig. 7). The CO_2 adsorption Gibbs energy is the lowest for the (100)

surface (–0.9 eV at 550 °C), which is consistent with the high coverage measured spectroscopically. CO* species, on the other hand, adsorb on oxygen and are less sensitive to the surface termination. For both CO_2* and CO*, a ceria lattice oxygen is significantly displaced and participates in forming bridge-like carbonate and carboxylate adsorbates [45]. For $Sm_{0.25}Ce_{0.75}O_{1.875}$/$CeO_{1.875}$(100) and (110), O-vacancy also acts as the anchoring site for oxygen in CO_2* and CO* (Supplementary Fig. 7). Finally, C* also adsorbs on the oxygen site forming typical CO-like species, while C* on the Ce site is considerably less stable by more than 4 eV. Fully oxidized CeO_2 are much less effective in stabilizing the carbonate, highlighting the importance of surface oxygen vacancies and/or Ce 4*f* localized electrons [27,41]. All species are stabilized by nearly identical amounts on the Sm-doped ceria $Sm_xCe_{1-x}O_{2-\delta}$ (100) surface, with Gibbs energies within 0.1 eV of $CeO_{2-\delta}$ (100) (see Supplementary Table 4 and Supplementary Fig. 14). Considering additional variations – higher oxygen vacancy concentration, including the Ni(111) surface, or varying the CO_2(g)/CO(g) pressures – does not affect the conclusions drawn from the Gibbs energy calculations (Figs. S11-S14).

For Ni, we simulated the bulk-truncated (111) and (211) surfaces. We find that while CO_2(g) adsorbs on the stepped Ni(211) surface in a weakly bonded bent mode (Fig. 4c), the adsorption Gibbs energy is highly unfavorable (ΔG = 2.0 eV). In addition, Ni(211) has a higher affinity for carbon adsorption than Ni(111) (Figs. S11-S14) [46]. Because C* binds on Ni, it is significantly more stable than on ceria (on which it binds on O) by 1.0 to 2.0 eV (Fig. 4c).

Using the calculated adsorption Gibbs free energies, we determined the surface-specific thermodynamic overpotentials required for the electroreduction reactions from CO_2(g) and CO(g) to C to be downhill in energy (see Supplementary Information). For $Sm_xCe_{1-x}O_{2-\delta}$ (100) and $CeO_{2-\delta}$ (100), this theoretical overpotential η is –530 and –610 mV, respectively, for the reduction of CO_2(g) to C and –504 and –460 mV, respectively, for the reduction of CO(g) to C. Both are significantly greater than the global thermodynamic overpotential for carbon deposition of –120 ±72 mV, which is in good agreement with our experimental observations. We also find that η

varies somewhat as a function of the surface termination from –530 mV to –630 mV for the reduction of CO_2(g) to C on oxygen deficient (111) and (110), respectively (Supplementary Table 3). Nonetheless, the theoretical values are in good agreement with the experimental potentials between –300 mV and –600 mV obtained via spectroscopic measurements (Fig. 1l). In contrast to ceria, for Ni(211), theoretical calculations predict a η value of –110 mV for CO_2(g) or CO(g) reduction to C. We note that, because the CO_2* adsorption Gibbs energy is very high on Ni, carbon deposition likely proceeds from CO(g).

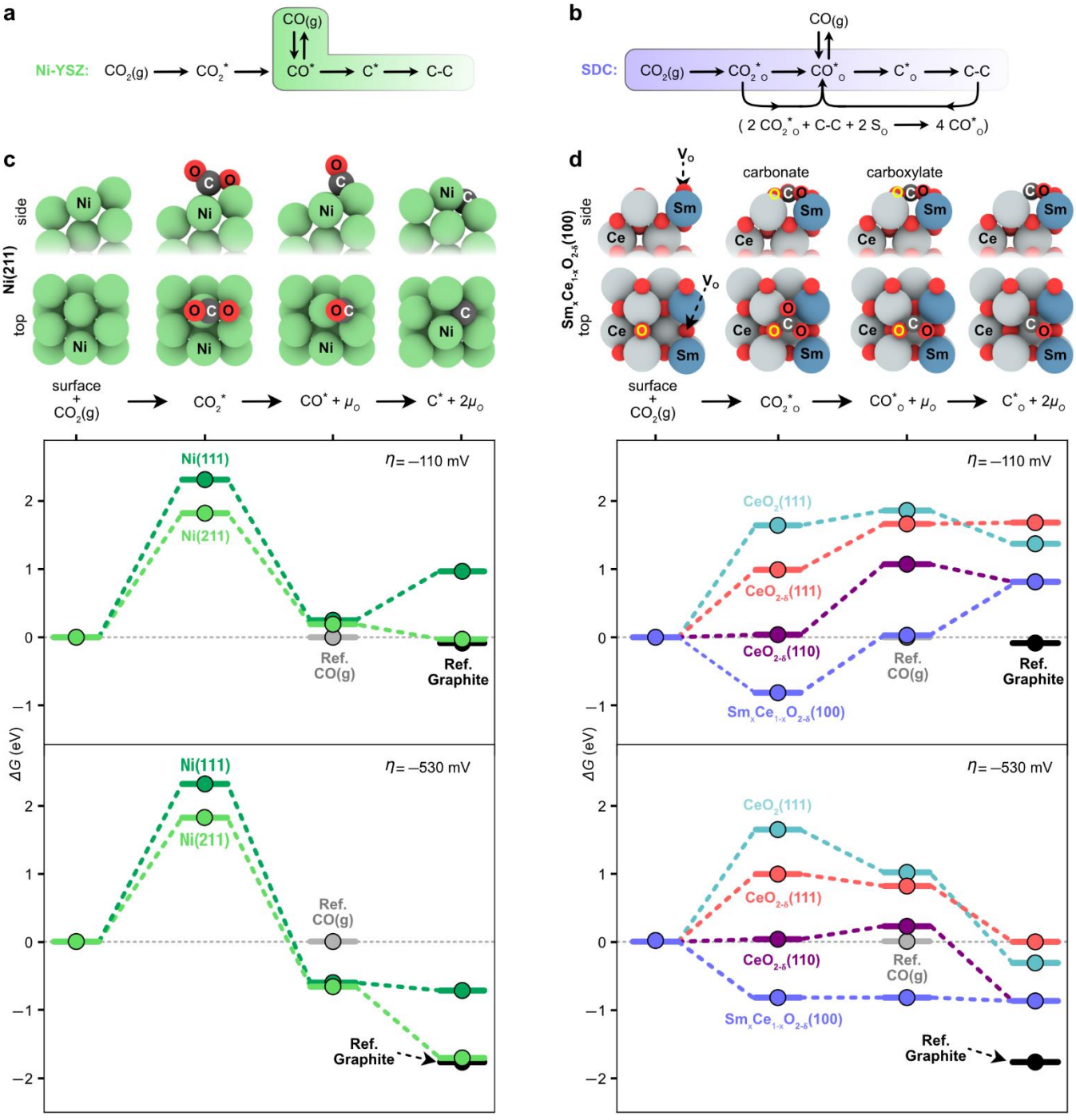

Fig. 4. Proposed reaction mechanism and calculated energetics for carbon formation on nickel and ceria surfaces. **a-b**, Reaction pathways for Ni-YSZ and SDC. **c-d**, Calculated free energy diagrams for Ni, $Sm_xCe_{1-x}O_{2-\delta}$ (100) and $CeO_{2-\delta}$ relative to the initial surfaces with gas-phase CO_2 and CO and oxidized carbon adsorbates under experimental conditions at overpotentials –110 mV and –530 mV. Structural evolution of the adsorbates on $Sm_xCe_{1-x}O_{2-\delta}$ (100) and Ni(211) surfaces is also shown, where the flat-laying carbonate species and bent CO_2 are stabilized via favorable oxygen bonding at the vacancy site. The yellow "O" labels on oxygen atoms indicate oxygen from

294 the ceria surface. Computational details and plots at other overpotential values are included in the
295 Supplementary Information (Supplementary Fig. 8-9).
296
297 With these experimental and computational results at hand, the mechanism for ceria's
298 carbon tolerance emerges. While the global reactions ($CO_2(g) \rightarrow C + 2(O^{2-}_{YSZ} - 2e^-_{CC})$ and $CO(g)$
299 $\rightarrow C + (O^{2-}_{YSZ} - 2e^-_{CC})$) are downhill at overpotentials of –73 mV and –146 mV (see
300 Supplementary Information and Supplementary Fig. 1), significant thermodynamic energy
301 differences between CO_2*, CO* and C* at those potentials suppress the reaction. As shown in Fig.
302 4d for $Sm_xCe_{1-x}O_{2-\delta}$ (100) (blue trace), at –110 mV overpotential (near the global thermodynamic
303 carbon deposition threshold), CO_2*_O (carbonate) is by far the most stable, followed by $CO*_O$ (~0.1
304 eV) and finally by $C*_O$ (~1.0 eV above graphite). Importantly, because the energy barriers are
305 positive for the progressive reduction of the carbonate adsorbate, and $CO*_O$ has a negligible
306 adsorption energy with respect to CO(g), selective CO_2(g) reduction to CO(g) is expected. On the
307 other hand, in Fig. 4c, Ni(211) (green trace) exhibits precisely the opposite, with C* being the most
308 stable. APXPS shows identical trends in terms of adsorbate coverage for ceria. Here, the carbonate
309 and CO* trap the carbon, enabled by the large free energy difference between carbonate, CO* and
310 C* and hinders the reaction to proceed to the global equilibrium. Applying a cathodic overpotential
311 of –530 mV flattens the energy landscape such that the traps disappear (Fig. 4d blue trace), again
312 consistent with our observation that carbon eventually deposits at large overpotentials. The large
313 CO_2* adsorption energy is also crucial, as it establishes a high carbonate coverage (observed also in
314 APXPS) and could provide a driving force for the surface reverse-Boudouard reaction (ΔG_{rxn} = 0.31
315 eV for $CeO_{1.875}$(100)) to remove transiently deposited carbon (Fig. 4b). Thus, the two key
316 requirements for suppressing carbon deposition satisfied by $CeO_{1.875}$(100) are: (1) trapping carbon
317 in oxidized carbon intermediates, and (2) establishing a high carbonate coverage. We predict that
318 (100) and (110) surface terminations best satisfy these requirements (Fig. 4d). Higher oxygen

deficiency increases this effect (Supplementary Fig. 16). Hence, dependence on surface termination and oxygen vacancy concentration highlight the tunability of carbon suppression.

Technological demonstration with scaled-up cells

With these insights, we demonstrated technological feasibility by fabricating 16 cm^2 SOCs with nanostructured, porous Gd-doped ceria negative-electrodes and testing the carbon-tolerance of these scaled-up cells during CO_2 electrolysis operation at 750 °C (Fig. 5). For comparison, we also tested a state-of-the-art Ni-YSZ based cell in approximately identical conditions, for comparison [9]. Similar to the model electrodes, we increased the electrolysis current density stepwise until the cell voltage began to rapidly increase, indicating carbon deposition. The cell with Ni-YSZ electrode showed carbon deposition at an outlet CO partial pressure of ~73%, lower than the thermodynamic Boudouard threshold (78% CO, balance CO_2) [9,13] (Fig. 5a). As in the case of the model ceria electrode, the cell with porous ceria electrode was able to operate past the threshold. We proceeded to carry out CO_2 electrolysis to produce CO beyond the threshold for more than 10 h with stable cell voltage (Fig. 5b). We then probed the operating limit, which we found to be ~95% CO at the outlet (Fig. 5a), and we could subsequently recover performance by oxidizing the deposited carbon. Post-mortem SEM images showed a damaged Ni-YSZ electrode (delamination between electrode and electrolyte) and an intact ceria electrode (Fig. 5c). Considering also electrochemical carbon deposition rather than only Boudouard deposition, the driving force is even further past the threshold (Supplementary Fig. 10).

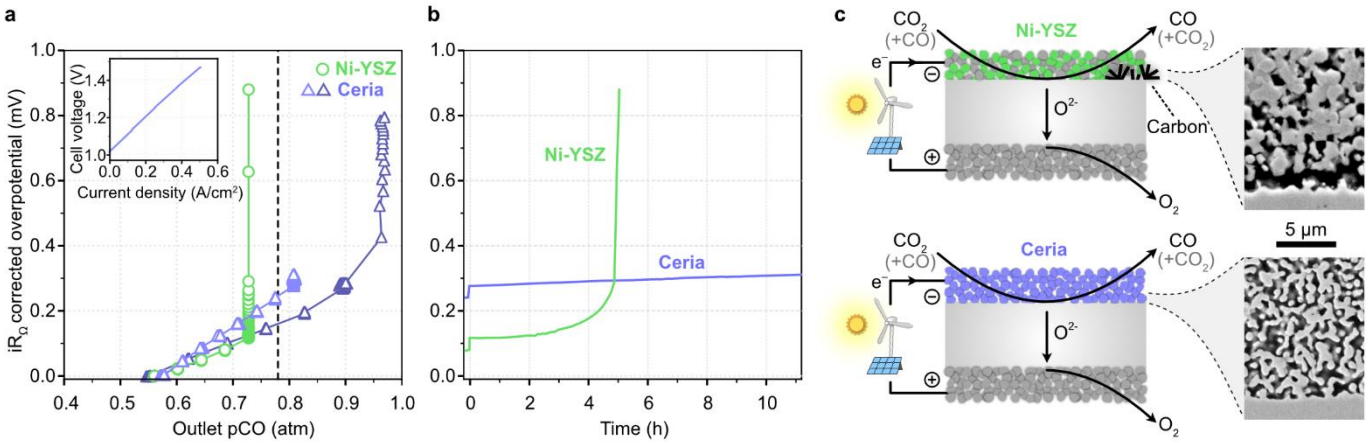

Fig. 5. Comparison of the abilities of scaled-up solid oxide cells with Ni-YSZ vs ceria electrodes to suppress carbon deposition during CO_2 electrolysis. a, Measured outlet CO partial pressure (balance CO_2) and cell overpotential corrected for ohmic potential drop (iR_Ω, where R_Ω is the ohmic area-specific resistance) at increasing applied current densities. The dashed vertical line is the thermodynamic threshold of carbon deposition via the Boudouard reaction. Inset: Typical electrolysis current-voltage curve measured on a cell with ceria negative-electrode. **b**, Part of the same data in **a**, now shown as a function of time at two of the final operating points (fixed current density, 0.35 A/cm^2 for the ceria cell and 0.5 A/cm^2 for the Ni-YSZ cell). **c**, Illustrations of the two cell types and post-test cross-sectional SEMs at the gas outlet near the negative-electrode/electrolyte interfaces where carbon deposited in the Ni-YSZ electrode and caused interface delamination. The cells had 16 cm^2 active area and were operated at 750 °C and 1 atm pressure in a plug-flow test configuration. Further test data is given in Supplementary Information and Supplementary Fig. 10.

The remarkable carbon-suppression capability of ceria, now rationalized in this work, has major implications for stable and selective CO_2 electrolysis. First, it offers robustness against a hard-failure mode that can immediately end device lifetime. Electrolysis on ceria electrodes may still be carried out in safe conditions, now with the insurance that the electrolyzer can survive operational accidents. Eliminating the risk of cell death could have major impact on commercial CO and fuel production device economics and could be especially beneficial for mission-critical applications, such as solid oxide CO_2 electrolyzers that will be used on Mars (to be first demonstrated on NASA's 2020 rover mission). Second, it is possible to push operation into conventionally unsafe conditions and thereby obtain higher yields of fuel and O_2 product. The

ability to achieve a higher CO concentration, which is limited to well below 50% in today's cell stacks due to thermodynamics and gradients [9], would reduce the cost of downstream separation to obtain a pure CO product.

The next step towards full-scale CO_2 electrolysis technology is integration of these nickel-free, nanostructured ceria electrodes into alternative cell designs that provide improved electronic current collection and lower overall cell resistance than the electrolyte-supported cells used in this demonstration. Metal-supported or oxygen-electrode-supported cells with thin electrolytes are candidates that do not rely on nickel for structural support and current collection, unlike the majority of cells being developed.

Finally, the new mechanistic understanding gained from our *operando* spectroscopy experiments and DFT modeling will guide the tuning of the surface properties of ceria and other vacancy-rich oxides to further improve carbon-tolerance. More generally, our insights and approach could contribute to achieving stable and selective catalytic reactions involving carbon chemistry.

Methods

Preparation of Model Electrode Cells

The single-chamber model electrochemical cells were fabricated on single-crystal (100) $Y_{0.16}Zr_{0.84}O_{1.92}$ (YSZ) substrates acting as the oxygen-ion-conducting electrolyte with dimensions 10 x 10 x 0.5 mm^3, with one side polished. The fabrication procedure follows in chronological order. The counter-electrode (CE) was applied on the rough side of the substrate by hand-painting Pt paste (Ferro GmbH 64021015), which was dried on a hot-plate at 200 °C and sintered at 800 °C for 1 h in stagnant air, forming a porous Pt backbone. Next, an aqueous precursor salt solution for Pr-doped ceria (PDC) [33] was wet infiltrated, dried at 250 °C on a hot-plate and decomposed at 350 °C for 0.5 h in stagnant air. The PDC was introduced to enhance the oxygen-ion-conducting and electrocatalytic capabilities. The large area and relatively high performance of the CE ensured that the prevalent part

of the potential-drop was across the working-electrode (WE), with a minor (<1 %) drop over the electrolyte. The exact overpotential of the CE was not determined, but assumed to be insignificant. The overpotential of the WE was thus estimated as $\eta_{WE} = V_{cell} - I_{cell}R_{\Omega}$, with R_{Ω} found by electrochemical impedance spectroscopy (EIS). On the polished side, the Pt or Ni current conducting pattern was fabricated by metal lift-off photolithography. An undercut resist layer (Dow Microposit LOL 2000) was spin-coated on the polished side of the YSZ substrate at 2000 r.p.m. for 60 s (~300nm thick) and annealed in air at 180 °C for 5 minutes. To the annealed undercut layer, a positive photoresist (Shipley S-1813) was spin-coated at 4000 r.p.m. for 45 s and baked at 100 °C for 2.5 min underneath a glass cover. The photomask was aligned with a Karl Suss MJB 3 mask aligner and the spin-coated films were exposed to UV light with a dosage of 105 mJ. The photoresist was developed in a Shipley Microposit MF CD-26 Developer solution until the undercut was ~1 μm. After the pattern was rinsed with deionized water, dried, oxygen plasma cleaned for 30 secs at 200 W, the metal was deposited in 2250 mTorr Ar in a DC magnetron Lesker sputter system. Liftoff was accomplished dissolving the resist in Baker PRS-1000 Positive Photoresist stripper heated to 50 °C. A final oxygen plasma treat at 300 W for 60s ensured removal of any photolithographic residue. The Pt pattern current collector consisted of 27 x 2000 µm stripes of 180 nm height and 5 µm width separated by 10 µm. A closed loop design improved interconnectivity to prevent disconnected metal stripes due to defects in the photolithography process; 500 x 750 μm^2 Pt contact pads were placed on the side of the patterns for contact with the current collector probe (Supplementary Fig. 11). The Ni pattern consisted of 13 x 2000 µm stripes of 200 nm height and 5 µm width separated by 50 µm. A closed loop design was used again to ensure metal connectivity. A 500 x 750 μm^2 Ni contact pad was placed at one end of the pattern for probe contact. Each YSZ patterned sample had two WEs so that the biased electrode could be compared to a reference sample exposed to identical experimental conditions but left unbiased. The Pt was annealed at 650 °C for 1 h in 100 mTorr, On the Pt pattern samples, a 650 µm thick $Sm_{0.2}Ce_{0.8}O_{1.9-\delta}$ (SDC) film was deposited by pulsed-laser deposition at 650 °C in 5 mTorr O_2 with a laser fluency of 1.5 J cm^{2-} at 10 Hz with a substrate to target distance of 70

cm. For the Ni-SDC sample, an additional 35 nm thick NiO layer was deposited by PLD on top of the SDC. The NiO layer was reduced to randomly dispersed, approximately 200-400 nm, Ni particles in-situ during the XPS experiment with a 500 mTorr $CO:CO_2$ (1:1) atmosphere. The Ni-YSZ sample had Ni particles next to the Ni pattern, which varied in size from 40 nm to less than 1 nm.

Electrochemical XPS

Ambient-pressure XPS experiments were conducted at beamline 9.3.2 [47] (Ni-SDC and SDC samples) and beamline 11.0.2 [48] (Ni-YSZ sample) at the Advanced Light Source synchrotron, Lawrence Berkeley National Laboratory. Scienta R4000 HiPP and Specs Phoibos 150 differentially pumped electron analyzers are employed for beamline 9.3.2 and 11.0.2, respectively, which together with a homebuilt sample holder (Supplementary Fig. 11) allows for experimental conditions of up to 700 °C [49] and 1000 mTorr [47], or several thousand mTorr for 11.0.2. Ohmic heating was supplied by a ceramic heater. Electrical contact was established by mechanically pressing a Pt coil onto the CE, while the electrical contact to the WE was made by Pt/Ir probes. More details on the design of the sample holder can be found elsewhere [48,49].

A similar kinetic energy was applied, when possible, namely 160 – 320 eV. Incident angle from the sample normal was 75 ° for the SDC and Ni-SDC samples at beamline 9.3.2, while it was 65 ° for Ni-YSZ at beamline 11.0.2. This and other differences between the two beam-lines, such as width of incident beam and distance between sample and the aperture, causes significantly different gas phase peak intensity between the samples, and a slightly different gas phase BE as seen in Supplementary Fig. 4. This did however not affect the data analysis significantly. The WE and an Au foil were Fermi coupled with the electron analyzer. The BE of each spectrum at OCV was calibrated with the Au $4f_{7/2}$ peak (84.0 eV). A Biologic SP-300 potentiostat was used for chrono-amperometry and EIS. The latter was used to estimate the temperature by comparing the ohmic resistance, R_Ω, to that measured during a calibration experiment. R_Ω of a similar sample on the same sample holder was measured in a tube

furnace in 500 mTorr O_2 and correlated to the temperature measured with a thermocouple. The thermal conductivity of O_2 is similar to that of CO and CO_2, but the different gas atmosphere does introduce some uncertainty. A change in total pressure from 500 mTorr to 50 mTorr, which far exceeds the uncertainty during the experiments, correspond to a temperature uncertainty of ±7 °C. During the experiments at 550 °C, the heater was used to adjust R_Ω with an accuracy of ±100 Ω, which translates to an additional uncertainty of ±3 °C. Thus, a total uncertainty in temperature measurements is estimated to no more than ±10 °C.

During the experiments, adventitious carbon was first burned off for the SDC and NiO-SDC samples by flowing O_2 at 550 °C. This was not possible for the Ni-YSZ sample, as the metallic Ni pattern would undergo a redox cycle to NiO potentially causing an electrical disconnection of part of the electrode. CO and CO_2 of research grade purity was then carefully dosed and equilibrated to a ~1:1 ratio, which was confirmed by means of the XPS gas phase peaks intensities calibrated for the difference in electron-molecule scattering cross-sections of CO and CO_2 [50], as well as with a residual gas analyzer.

Density Functional Theory

DFT calculations were performed within the Hubbard-U method (DFT+U) using the Vienna Ab initio Simulation Package (VASP, version 5.4.1) using the nearly identical settings as in our recent paper on CeO_2 [51]. The use of PAW potentials, 500 eV plane-wave cutoff, U_{eff}(Ce, Sm) = 4.5 eV [52,53] and dense (9x9x9) k-point grid resulted in the equilibrium lattice parameter of a = 5.497 Å for CeO_2 and a = 3.52 Å for Ni . Our simulation cells for ceria surfaces contained a minimum of 3 layers (and 4 for Ni surfaces) with a 2x2 (3x2) periodicity. The two topmost layers were always allowed to relax until the forces were lower than 0.02 eV A^{-1} using a 5x5x1 k-point mesh.

In the CeO_2 DFT calculations, the top-only surface oxygen vacancy concentration [V_O] is held fixed at zero for "CeO_2 (111)", at 25% for "$CeO_{2-\delta}$ (1xx)" (x being 0 or 1) or "$CeO_{2-\delta}$ (1xx)|25% V_O", or at

50% for "$CeO_{2-\delta}$ (111)|50% V_O" in Supplementary Fig. 7-9 and Supplementary Fig. 14-18, and [V_O] is not affected by applied overpotential. In reality, CO_2* and [V_O] vary with overpotential [27].

Because of the elevated temperature nature of CO_2 electrolysis in SOCs (823 K in this work), we include vibrational entropy as well as configurational entropy of gas molecules, which affects the calculated free energies significantly relative to T = 0 K enthalpy values, Supplementary Tables 4 and 5. Using these calculated adsorption energies, we determined the overpotentials required for the electrochemical reduction reactions from CO_2(g) and CO(g) to C, defined as the potential at which the C* becomes exergonic with respect to the previous reaction steps. When a cathodic overpotential is applied, CO* free energy is shifted down by 2eη and C* by 4eη, where η is the theoretical overpotential. We rationalize using a thermodynamic approach because reasonable kinetic rates (~1 $site^{-1}s^{-1}$) are expected for barriers as large as 2 eV at the operating temperature of 800 K [54].

Scaled-up cells

Two cells of different type with 16 cm^2 active area were tested: one nickel-electrode reference cell and one carbon-tolerant ceria-electrode cell. Both cells were tested in a plug-flow set-up [55] with pO_2 sensors just upstream and downstream of the cell, placed into the fuel-side gas flow. These pO_2 values were used, together with leak analysis, to quantify the outlet pCO. Absolute or positive pO_2 voltage values are used throughout; 1000 mV corresponds to a very small quantity of oxygen such as 10^{-20} atm. Photos of the experimental setup can be seen in Supplementary Fig. 11.

The reference cell was a state-of-the-art porous Ni-YSZ supported cell produced by Haldor Topsoe A/S. The dense ~10 µm thick electrolyte consisted of 8 mol% Y-doped zirconia (8YSZ) and a Gd-doped ceria (GDC) barrier layer, and the porous oxygen electrode was a composite of GDC and lanthanum-strontium-cobalt-ferrite. The Ni-3YSZ support was ~300 µm thick with a 10-30 µm active Ni-8YSZ electrode layer. The fuel gas compartment was sealed with gold to an alumina test house, and nickel and gold meshes functioned as current collectors and gas distributors for the fuel and oxygen side, respectively. After reduction of NiO to Ni at 850 °C and initial performance

characterization, the cell was tested with 14 L/h CO and 9 L/h CO_2, and a current density of 0.5 A/cm^2. Further details about this cell can be found in ref. [9].

The cell with enhanced carbon tolerance was a 150 µm thick dense 10Sc1CeSZ electrolyte-supported cell with a 35-50 µm thick porous GDC backbone sprayed on both sides (10Sc1CeSZ is ZrO_2 doped with 10 mol% Sc_2O_3 and 1 mol% CeO_2). The oxygen side was infiltrated with 3 cycles of an aqueous solution comprising 1.63 M metal nitrates corresponding to $La_{0.75}Sr_{0.25}MnO_3$. The cell was heated to 1000 °C to form that perovskite phase on the GDC backbone. The oxygen side was then infiltrated with 1 cycle of 3 M Ce and Pr nitrates solution with Ce:Pr 8:2 ratio (for forming PDC upon heating), and the fuel side was infiltrated with 1 cycle of a 3 M Ce and Gd nitrates solution with Ce:Gd 8:2 ratio, to enhance the electrochemical performance. The infiltration solutions were prepared from the respective metal nitrates mixed in DI water with a Triton X-100 surfactant. Pt-paste was used as a current-collection layer on both sides of the cell (Supplementary Fig. 11). The cell was mounted in a similar manner as the Ni-YSZ cell, but with a Pt mesh as the current collector and gas distributor on the fuel side (Supplementary Fig. 11). The cell was tested multiple times beyond the carbon deposition onset threshold. The gas flow used for Fig. 5 without carbon deposition was 7 L/h of CO and 4.5 L/h of CO_2 to the fuel side, and 40 L/h of O_2 to the oxygen side. The applied current density was 0.35 A/cm^2. The measured pO_2 of the outlet gas was 1031 mV, above the carbon deposition threshold of 1024 mV at the 750 °C operating temperature. For the test that showed cell voltage increase due to carbon deposition, the flow rates were 3.5 L/h CO and 2.25 L/h CO_2, with a current density of 0.3 A/cm^2. Including a minor cross-over leak, the resulting inlet gas at the cell had a pCO_2 of 40-45% (Fig. 5). The measured pO_2 of the outlet gas reached 1114 mV before the test was stopped. Prior CO_2 electrolysis works report testing with inlet pCO_2 ranging from 10% to 100% [1,5,8–10,13]. In a commercial system, a pCO_2 closer to 100% may be preferable and more realistic, however for nickel-containing electrodes the pCO_2 of the supplied gas must not be too close to 100% to avoid oxidation of the nickel. The test conditions here were chosen based on recent detailed high-temperature CO_2 electrolysis studies [9,13] to minimize concentration gradients and overpotentials and to begin (at open-

circuit condition) relatively close to the thermodynamic carbon deposition threshold (pCO_2 of 22%), ensuring that carbon deposition conditions could be reached without inducing other known degradation mechanisms that are driven by large gradients and overpotentials [7,9,13].

Data Availability

Data underlying the study can be found at https://figshare.com/s/792e4b1ea3e174a1f60d (APXPS and cell testing) and https://www.catalysis-hub.org/publications/SkafteOxidized2018 (DFT).

References:

1. Jensen, S. H., Larsen, P. H. & Mogensen, M. Hydrogen and synthetic fuel production from renewable energy sources. *Int. J. Hydrogen Energy* **32,** 3253–3257 (2007).
2. Graves, C., Ebbesen, S. D., Mogensen, M. & Lackner, K. S. Sustainable hydrocarbon fuels by recycling CO_2 and H_2O with renewable or nuclear energy. *Renew. Sustain. Energy Rev.* **15,** 1–23 (2011).
3. Seh, Z. W. *et al.* Combining theory and experiment in electrocatalysis: Insights into materials design. *Science* **355,** eaad4998 (2017).
4. Davis, S. J. *et al.* Net-zero emissions energy systems. *Science* **360,** eaas9793 (2018).
5. Bidrawn, F. *et al.* Efficient Reduction of CO_2 in a Solid Oxide Electrolyzer. *Electrochem. Solid-State Lett.* **11,** B167 (2008).
6. Jensen, S. H. *et al.* Large-scale electricity storage utilizing reversible solid oxide cells combined with underground storage of CO_2 and CH_4. *Energy Environ. Sci.* (2015).
7. Graves, C., Ebbesen, S. D., Jensen, S. H., Simonsen, S. B. & Mogensen, M. B. Eliminating degradation in solid oxide electrochemical cells by reversible operation. *Nat. Mater.* **14,** 239–244 (2015).

8. Hartvigsen, J., Elangovan, S., Elwell, J. & Larse, D. Oxygen Production from Mars Atmosphere Carbon Dioxide Using Solid Oxide Electrolysis. *ECS Trans.* **78,** 2953–2963 (2017).

9. Skafte, T. L., Blennow, P., Hjelm, J. & Graves, C. Carbon deposition and sulfur poisoning during CO_2 electrolysis in nickel-based solid oxide cell electrodes. *J. Power Sources* **373,** 54–60 (2018).

10. Duboviks, V. *et al.* A Raman spectroscopic study of the carbon deposition mechanism on Ni/CGO electrodes during CO/CO_2 electrolysis. *Phys. Chem. Chem. Phys.* **16,** 13063 (2014).

11. Helveg, S. *et al.* Atomic-scale imaging of carbon nanofibre growth. *Nature* **427,** 426–429 (2004).

12. Tao, Y., Ebbesen, S. D. & Mogensen, M. B. Carbon Deposition in Solid Oxide Cells during Co-Electrolysis of H_2O and CO_2. *J. Electrochem. Soc.* **161,** F337–F343 (2014).

13. Navasa, M., Frandsen, H. L., Skafte, T. L., Sundén, B. & Graves, C. Localized carbon deposition in solid oxide electrolysis cells studied by multiphysics modeling. *J. Power Sources* **394,** 102–113 (2018).

14. Homel, M., Gür, T. M., Koh, J. H. & Virkar, A. V. Carbon monoxide-fueled solid oxide fuel cell. *J. Power Sources* **195,** 6367–6372 (2010).

15. Boldrin, P. *et al.* Strategies for Carbon and Sulfur Tolerant Solid Oxide Fuel Cell Materials, Incorporating Lessons from Heterogeneous Catalysis. *Chem. Rev.* **116,** 13633–13684 (2016).

16. Murray, E. P., Tsai, T. & Barnett, S. A. A direct-methane fuel cell with a ceria-based anode. *Nature* **400,** 649–651 (1999).

17. Park, S., Vohs, J. M. & Gorte, R. J. Direct oxidation of hydrocarbons in a solid-oxide fuel cell. *Nature* **404,** 265–267 (2000).

18. Yang, L. *et al.* Enhanced Sulfur and Coking Tolerance of a Mixed Ion Conductor for SOFCs:

564 $BaZr_{0.1}Ce_{0.7}Y_{0.2-x}Yb_xO_{3-\delta}$. *Science* **326,** 126–129 (2009).

565 19. Li, X. *et al.* In Situ Probing of the Mechanisms of Coking Resistance on Catalyst-Modified
566 Anodes for Solid Oxide Fuel Cells. *Chem. Mater.* **27,** 822–828 (2015).

567 20. Choi, Y., Brown, E. C., Haile, S. M. & Jung, W. Electrochemically modified, robust solid
568 oxide fuel cell anode for direct-hydrocarbon utilization. *Nano Energy* **23,** 161–171 (2016).

569 21. Skafte, T. L., Sudireddy, B. R., Blennow, P. & Graves, C. Carbon and Redox Tolerant
570 Infiltrated Oxide Fuel-Electrodes for Solid Oxide Cells. *ECS Trans.* **72,** 201–214 (2016).

571 22. Irvine, J. T. S. *et al.* Evolution of the electrochemical interface in high-temperature fuel cells
572 and electrolysers. *Nat. Energy* **1,** 15014 (2016).

573 23. Rostrup-Nielsen, J. R. & Alstrup, I. Innovation and science in the process industry: Steam
574 reforming and hydrogenolysis. *Catal. today* **53,** 311–316 (1999).

575 24. Mortensen, P. M. & Dybkjær, I. Industrial scale experience on steam reforming of CO_2-rich
576 gas. *Appl. Catal. A Gen.* **495,** 141–151 (2015).

577 25. Guo, J. *et al.* Improving the Carbon Resistance of Ni-Based Steam Reforming Catalyst by
578 Alloying with Rh: A Computational Study Coupled with Reforming Experiments and
579 EXAFS Characterization. *ACS Catal.* **1,** 574–582 (2011).

580 26. Nikolla, E., Schwank, J. & Linic, S. Hydrocarbon steam reforming on Ni alloys at solid
581 oxide fuel cell operating conditions. *Catal. Today* **136,** 243–248 (2008).

582 27. Feng, Z. a., Machala, M. L. & Chueh, W. C. Surface electrochemistry of CO_2 reduction and
583 CO oxidation on Sm-doped CeO_{2-x}: coupling between Ce^{3+} and carbonate adsorbates. *Phys.*
584 *Chem. Chem. Phys.* **17,** 12273–12281 (2015).

585 28. Yu, Y. *et al.* CO_2 activation and carbonate intermediates: an operando AP-XPS study of CO_2
586 electrolysis reactions on solid oxide electrochemical cells. *Phys. Chem. Chem. Phys.* **16,**
587 11633–11639 (2014).

29. Cheng, Z., Sherman, B. J. & Lo, C. S. Carbon dioxide activation and dissociation on ceria (110): A density functional theory study. *J. Chem. Phys.* **138,** 1–20 (2013).

30. Zhang, C. *et al.* Measuring fundamental properties in operating solid oxide electrochemical cells by using in situ X-ray photoelectron spectroscopy. *Nat. Mater.* **9,** 944–949 (2010).

31. Opitz, A. K. *et al.* Surface Chemistry of Perovskite-Type Electrodes During High Temperature CO_2 Electrolysis Investigated by Operando Photoelectron Spectroscopy. *ACS Appl. Mater. Interfaces* **9,** 35847–35860 (2017).

32. Chueh, W. C., Hao, Y., Jung, W. & Haile, S. M. High electrochemical activity of the oxide phase in model ceria–Pt and ceria–Ni composite anodes. *Nat. Mater.* **11,** 155–161 (2012).

33. Graves, C., Martinez, L. & Sudireddy, B. R. High Performance Nano-Ceria Electrodes for Solid Oxide Cells. *ECS Trans.* **72,** 183–192 (2016).

34. Yu, Y. *et al.* Carbon Deposits and Pt/YSZ Overpotentials in CO/CO_2 Solid Oxide Electrochemical Cells. *ECS Trans.* **57,** 3119–3126 (2013).

35. Morar, J. F. *et al.* C 1s excitation studies of diamond (111). I. Surface core levels. *Phys. Rev. B* **33,** 1346–1349 (1986).

36. Haerle, R., Riedo, E., Pasquarello, A. & Baldereschi, A. sp^2/sp^3 hybridization ratio in amorphous carbon from C 1s core-level shifts: X-ray photoelectron spectroscopy and first-principles calculation. *Phys. Rev. B* **65,** 045101 (2001).

37. Ermolieff, A. *et al.* XPS, Raman spectroscopy, X-ray diffraction, specular X-ray reflectivity, transmission electron microscopy and elastic recoil detection analysis of emissive carbon film characterization. *Surf. Interface Anal.* **31,** 185–190 (2001).

38. Alzate-Restrepo, V. & Hill, J. M. Carbon deposition on Ni/YSZ anodes exposed to CO/H_2 feeds. *J. Power Sources* **195,** 1344–1351 (2010).

39. El Gabaly, F., McCarty, K. F., Bluhm, H. & McDaniel, A. H. Oxidation stages of Ni

612 electrodes in solid oxide fuel cell environments. *Phys. Chem. Chem. Phys.* **15,** 8334 (2013).

613 40. Mudiyanselage, K. *et al.* Importance of the Metal-Oxide Interface in Catalysis: In Situ
614 Studies of the Water-Gas Shift Reaction by Ambient-Pressure X-ray Photoelectron
615 Spectroscopy. *Angew. Chemie - Int. Ed.* **52,** 5101–5105 (2013).

616 41. Staudt, T. *et al.* Electronic Structure of Magnesia-Ceria Model Catalysts, CO_2 Adsorption,
617 and CO_2 Activation: A Synchrotron Radiation Photoelectron Spectroscopy Study. *J. Phys.*
618 *Chem. C* **115,** 8716–8724 (2011).

619 42. Czekaj, I. *et al.* Characterization of surface processes at the Ni-based catalyst during the
620 methanation of biomass-derived synthesis gas: X-ray photoelectron spectroscopy (XPS).
621 *Appl. Catal. A Gen.* **329,** 68–78 (2007).

622 43. Ming, H. *et al.* Large scale electrochemical synthesis of high quality carbon nanodots and
623 their photocatalytic property. *Dalt. Trans.* **41,** 9526 (2012).

624 44. Paier, J., Penschke, C. & Sauer, J. Oxygen Defects and Surface Chemistry of Ceria: Quantum
625 Chemical Studies Compared to Experiment. *Chem. Rev.* **113,** 3949–3985 (2013).

626 45. Vayssilov, G. N., Mihaylov, M., Petkov, P. S., Hadjiivanov, K. I. & Neyman, K. M.
627 Reassignment of the Vibrational Spectra of Carbonates, Formates, and Related Surface
628 Species on Ceria: A Combined Density Functional and Infrared Spectroscopy Investigation.
629 *J. Phys. Chem. C* **115,** 23435–23454 (2011).

630 46. Bengaard, H. S. *et al.* Steam Reforming and Graphite Formation on Ni Catalysts. *J. Catal.*
631 **209,** 365–384 (2002).

632 47. Grass, M. E. *et al.* New ambient pressure photoemission endstation at Advanced Light
633 Source beamline 9.3.2. *Rev. Sci. Instrum.* **81,** (2010).

634 48. Frank Ogletree, D., Bluhm, H., Hebenstreit, E. D. & Salmeron, M. Photoelectron
635 spectroscopy under ambient pressure and temperature conditions. *Nucl. Instruments Methods*

Phys. Res. Sect. A Accel. Spectrometers, Detect. Assoc. Equip. **601,** 151–160 (2009).

49. Whaley, J. a. *et al.* Note: Fixture for characterizing electrochemical devices in-operando in traditional vacuum systems. *Rev. Sci. Instrum.* **81,** 1–3 (2010).

50. Hwang, W., Kim, Y.-K. & Rudd, M. E. New model for electron-impact ionization cross sections of molecules. *J. Chem. Phys.* **104,** 2956 (1996).

51. Balaji Gopal, C. *et al.* Equilibrium oxygen storage capacity of ultrathin $CeO_{2-\delta}$ depends non-monotonically on large biaxial strain. *Nat. Commun.* **8,** 15360 (2017).

52. Fabris, S., de Gironcoli, S., Baroni, S., Vicario, G. & Balducci, G. Reply to "Comment on 'Taming multiple valency with density functionals: A case study of defective ceria'". *Phys. Rev. B* **72,** 237102 (2005).

53. Farra, R. *et al.* Promoted Ceria: A structural, catalytic, and computational study. *ACS Catal.* **3,** 2256–2268 (2013).

54. Nørskov, J. K., Studt, F., Abild-Pedersen, F. & Bligaard, T. *Fundamental Concepts in Heterogeneous Catalysis*. *Fundamental Concepts in Heterogeneous Catalysis* (John Wiley & Sons, Inc, 2014).

55. Jensen, S. H., Hauch, A., Hendriksen, P. V. & Mogensen, M. Advanced Test Method of Solid Oxide Cells in a Plug-Flow Setup. *J. Electrochem. Soc.* **156,** B757 (2009).

Acknowledgments: We thank Liming Zhang for SEM assistance, Anne Lyck Smitshuysen for assistance with preparing the large-format cells, and Hendrik Bluhm for assistance at beamline 11.0.2. This research used resources of the Advanced Light Source, which is a DOE Office of Science User Facility under contract no. DE-AC02-05CH11231.

The authors gratefully acknowledge financial support from Haldor Topsoe A/S, Innovation Fund Denmark, the Danish Agency for Science, Technology and Innovation (grant no. 5176-00001B and 5176-00003B), and Energinet.dk under the project ForskEL 2014-1-12231. M.B. acknowledges

support from by the U.S. Department of Energy, Chemical Sciences, Geosciences, and Biosciences (CSGB) Division of the Office of Basic Energy Sciences, via Grant DE-AC02-76SF00515 to the SUNCAT Center for Interface Science and Catalysis. We thank J. Nørskov and T. Bligaard at SUNCAT Center for Interface Science and Catalysis for hosting T.L.S. and C.G. All calculations in this work were performed with the use of the computer time allocation (m2997) at the National Energy Research Scientific Computing Center, a DOE Office of Science User Facility supported by the Office of Science of the U.S. Department of Energy under Contract No. DE-AC02-05CH11231.

Author contributions: T.L.S, C.G. and W.C.C designed the experiments. T.L.S. carried out the spectroscopic and electrochemical analysis. M.L.M., L.M., E.S., S.S., and T.L.S. manufactured samples. T.L.S., Z.G. and C.G. carried out preliminary experiments and sample characterization. Z.G., T.L.S., C.B.G., M.M, C.G., M.L.M., and E.J.C. carried out the XPS experiments. M.B. and M.G.-M. designed and conducted the DFT calculations. T.L.S. and C.G. carried out the large-format cell experiments. T.L.S., C.G., W.C.C., M.B., M.G.-M., J.A.G.T., Z.G., and M.M. contributed to writing the article. C.G. initiated the collaborative project. W.C.C and C.G. supervised and guided the work.

Competing interests: Authors declare no competing interests.

Supplementary Information for

Selective high-temperature CO_2 electrolysis enabled by oxidized carbon intermediates

Theis L. Skafte, Zixuan Guan, Michael L. Machala, Chirranjeevi B. Gopal, Matteo Monti, Lev Martinez, Eugen Stamate, Simone Sanna, Jose A. Garrido Torres, Ethan Crumlin, Max García-Melchor, Michal Bajdich *, William C. Chueh * and Christopher Graves *

Calculations of electrochemical threshold

The carbon formation threshold on account of the Boudouard reaction can be found from thermodynamics:

$$\Delta G_r = \Delta H_r - T\Delta S_r = -RT\ln(K_r) = -RT\ln\left(\frac{pCO^2}{pCO_2}\right) \quad (1)$$

Where ΔG_r, ΔH_r and ΔS_r are the changes in Gibbs energy, the enthalpy and the entropy of the reaction, respectively. T is the absolute temperature, R is the gas constant, K_r is the equilibrium constant of the reaction, and pCO and pCO_2 are the CO and CO_2 partial pressures. Since we only have CO and CO_2 in the atmosphere, the mole fraction of CO is given by $x_{CO} = 1 - x_{CO_2}$. If we now account for the total pressure, $p = pCO + pCO_2$, we then have:

$$K_x = K_{eq.} \cdot p = \frac{(1-x_{CO_2})^2}{x_{CO_2}} \quad (2)$$

The binomial solution to two equations with two unknowns can now be found:

$$x_{CO_2} = \left(\frac{1/2}{p\cdot K_{eq.}} + 1\right) - \sqrt{\left(\frac{1/2}{p\cdot K_{eq.}} + 1\right)^2 - 1} \quad (3)$$

$K_{eq.}$ is dependent on T, and can be found using FactSage thermochemical software and database [1].

The reactant gas atmosphere for the threshold can then be converted to a partial oxygen pressure, $pO_2(\text{Boud.})$, with the unit atm:

$$pO_2(\text{Boud.}) = 10^{2\cdot\log_{10}(K_{eq.})} \cdot \left(\frac{x_{CO_2}}{x_{CO}}\right)^2 \quad (4)$$

In the same manner, the pO_2 of the actual inlet reactant gas atmosphere, $pO_2(\text{reac.})$, can be calculated. Here, the equilibrium constant for the CO_2-electrolysis reaction; $CO_2 \rightleftharpoons CO + \frac{1}{2}O_2$, must be used. Since we now know the pO_2 of the inlet gas, we can use the Nernst equation to calculate the open-circuit voltage (OCV):

$$OCV = \frac{RT}{nF}\ln\left(\frac{pO_2(\text{air})}{pO_2(\text{reac.})}\right) \quad (5)$$

Where n is the number of electrons participating in the reaction, F is Faraday's constant, and $p\mathrm{O}_2(\mathrm{air})$ is the partial oxygen pressure of air (0.21 atm). The unit will be V.

In a similar manner, the potential of the threshold can be calculated, and by subtraction we find the electrochemical overpotential of the cell required for carbon formation:

$$\eta(\mathrm{Boud.}) = \mathrm{OCV} - \frac{RT}{\mathrm{n}F}\ln\left(\frac{p\mathrm{O}_2(\mathrm{air})}{p\mathrm{O}_2(\mathrm{Boud.})}\right) \quad (6)$$

Which will be negative (cathodic) given the experimental conditions chosen in the experiments. The relative contribution of the working electrode (WE), the counter electrode (CE) and the electrolyte was further elaborated on in the Materials and Methods section.

The same calculations can be carried out for the electrochemically driven carbon deposition reactions, with the appropriate thermodynamic data applied. Finally, we can plot the Nernst potential for each reaction, as well as the required overpotential for all three carbon deposition reactions. As seen in Supplementary Fig. 1, at the specific experimental conditions (250 mTorr CO, 250 mTorr CO_2, 550 °C), electrochemical carbon formation from CO_2 is thermodynamically favored at -73 mV overpotential, while electrochemical carbon formation from CO and the Boudouard reaction require a somewhat similar overpotential, -146 mV and -122 mV, respectively. At the experimental conditions for the SDC sample (75 mTorr CO, 75 mTorr CO_2, 550 °C), the three overpotential values are -94 mV, -189 mV, and -164 mV respectively (not shown in Supplementary Fig. 1). Considering these ranges of values and the maximum temperature uncertainty, the overpotential thresholds are overall within the range -120 $\pm$72 mV. All thermodynamic data used are for graphite as the reaction product – other carbon allotropes exhibit slightly different energetics, e.g. amorphous carbon has up to 15 kJ/mol larger formation energy, which corresponds to 39 mV or 78 mV more negative overpotential depending on the deposition reaction.

Photoemission spectra fitting and peak assignment

For all three samples the fitting routine was consistent, albeit with minor differences. The fitting software was CasaXPS v2.3.17PR1.1. All peaks were fitted with a symmetric Gaussian-Lorentzian shape, "GL(30)", except for sp^2 type carbon, which was fitted with an asymmetric peak consisting of a blend of a Doniach-Sunjic function and a Gaussian-Lorentzian function, "DS(0.03,125)GL(30)" [2,3]. This is due to the screening of electron-hole pair excitations at the Fermi level [4]. A singularity index of 0.03 was found to fit the data well, a value smaller than what others have reported using, i.e. 0.1-0.2 [2,5]. For SDC and Ni-SDC a Shirley background was fitted and subtracted, while for Ni-YSZ a linear background was deemed more suitable for the data. Changing the background type did not alter the results of the analysis, only the fitting error bars. Before and after each experimental condition, a spectrum for each relevant photon energy was collected on an Au foil a few mm from the sample, which was Fermi coupled (grounded) to the working electrode. Thus, all spectra were calibrated to Au $4f_{7/2}$ (84.0 eV). The photon energy was chosen such that the kinetic energy yielded an information depth of ~0.6 nm for all spectra (kinetic energy ~250 eV ±100 eV). The binding energies (BE) mentioned in the following refer to OCV, since the BE will shift with applied potential for some species.

C 1s. Despite the reduction in possible species due to the lack of H-, N- and F-atoms, there are still a significant amount of possible surface species to identify within a narrow BE window. In order of descending BE, the assigned peaks can be seen in Supplementary Table 1. In addition to these, an unidentified peak was often visible 1 eV higher than CO_2 (gas). The CO_2* and CO* peaks were assigned based on the reported BE in literature, e.g. Feng et al. [6]. CO_2* was not present on the Ni-YSZ electrode, and CO* only to a small degree. At the beginning of the test at OCV, adventitious C-C sp^2 was only present on Ni-YSZ. After carbon deposition at cathodic overpotentials, C-C sp^2 appeared to a minor degree on SDC and Ni-SDC, but the primary C-C type formed on these samples was sp^3.

O 1s. The assigned peaks can be seen in Supplementary Table 2. The C adsorbate peak could be either CO_3^{2-}, C=O, O-C=O, C-O-C or C-O-C=O, but this peak was only present for the SDC and Ni-SDC samples, not the Ni-YSZ. This is consistent with the lack of CO_3^{2-} (CO_2*) and to a certain extent, CO*, on Ni-YSZ in the C 1s spectra.

Other surface species, e.g. Zr 3d, Ce 4d, Ni 2p and 3p are of lower importance in the present study. These are simply fitted with sufficient peaks to accurately determine the BE shifting of the main peak while varying the potential (Supplementary Fig. 5 and Supplementary Fig. 20).

Current-potential curves

The current response during the chrono-amperometry experiments for the three samples is shown in Supplementary Fig. 12. The SDC sample in Supplementary Fig. 12a has a relatively low performance before applying a large cathodic potential of -600 mV. The activation is clearly visible by comparing the current at +200 mV anodic potential before and after the large cathodic bias. This sort of activation was expected to occur when the ceria surface was reduced sufficiently to cause crack-formation along the Pt-patterns. The formation of such cracks are confirmed by SEM after the experiment. This phenomenon is expected to significantly increase the surface area, which is not accounted for in the geometric area normalized current density shown here. More interestingly, a large increase in resistance of the cell is observed at the most reducing conditions. This is most likely due to coverage of the SDC surface by carbon [7], effectively blocking the 2PB, supported by an observed decrease in the lattice oxygen peak from O 1s.

For the Ni-SDC sample, Supplementary Fig. 12b, more current-potential points were collected. Like SDC, the resistance increased at the most reducing condition. This was followed by activation upon returning to the most oxidizing condition. The reason for this is unclear. The increased resistance at the reducing condition clearly shows hysteresis in the iV-curve. Such hysteresis is also observed for full-sized commercial SOECs during chrono-potentiometry experiments with carbon formation [8]. After oxidizing most of the carbon and returning to the reducing condition, the electrochemical performance is regained. We also applied negative bias to this electrode again and the same resistance increase was observed as the carbon grew back again (not shown).

Curiously, the formation of carbon did not cause an increase in resistance for the Ni-YSZ sample. The coverage of reaction sites by carbon might be compensated by electronically connecting more Ni particles as carbon is growing. This would increase the 3PB length and the performance.

The shape of the iV curves of the SDC samples (Supplementary Fig. 12a, b) are as expected based on comparison to other model electrode tests [6,9]. However, a reversed cathodic shape of the iV-curve for the Ni-YSZ sample was expected [9]. This might be due to the effect suggested above where carbon deposition extended the 3PB length, improving the electrode performance.

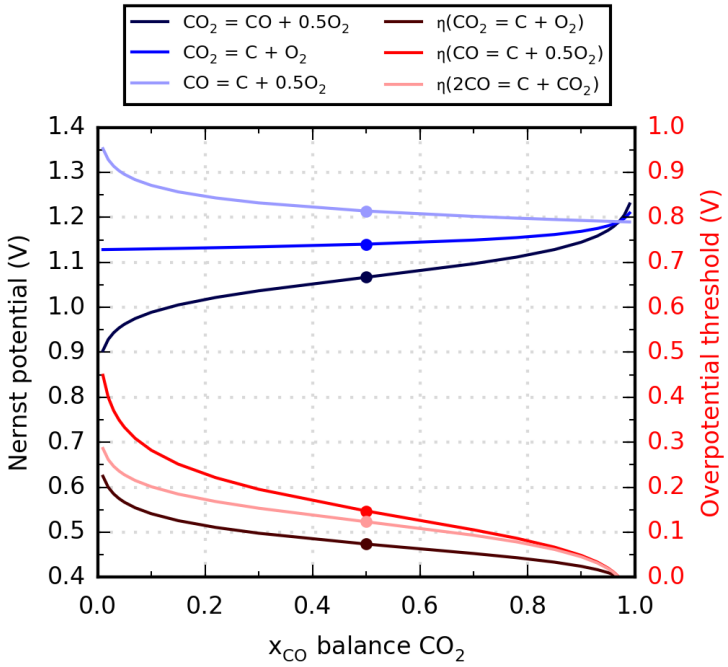

Supplementary Fig. 1.

Nernst potentials and overvoltage thresholds for CO_2 electrolysis and possible carbon formation reactions. The Nernst potential under changing concentration of CO in CO_2 at the specific experimental conditions (500 mTorr total pressure, 550 °C) is calculated for the CO_2 electrolysis reaction, and the reactions for electrochemical carbon formation from either CO_2 or CO. On the second y-axis, the overpotential thresholds for the two electrochemical carbon formation reactions and for the Boudouard reaction are plotted. Dots indicate the operating point for the APXPS experiments.

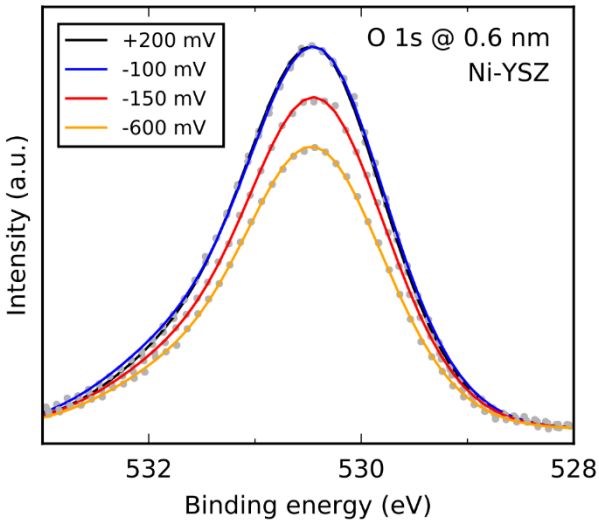

Supplementary Fig. 2.

Lattice oxygen (1s) XPS peak decreasing in intensity as carbon is deposited on the Ni-YSZ model electrode. The decrease in intensity indicates coverage of the YSZ surface. Shifts in BE due to the applied potential has here been corrected for.

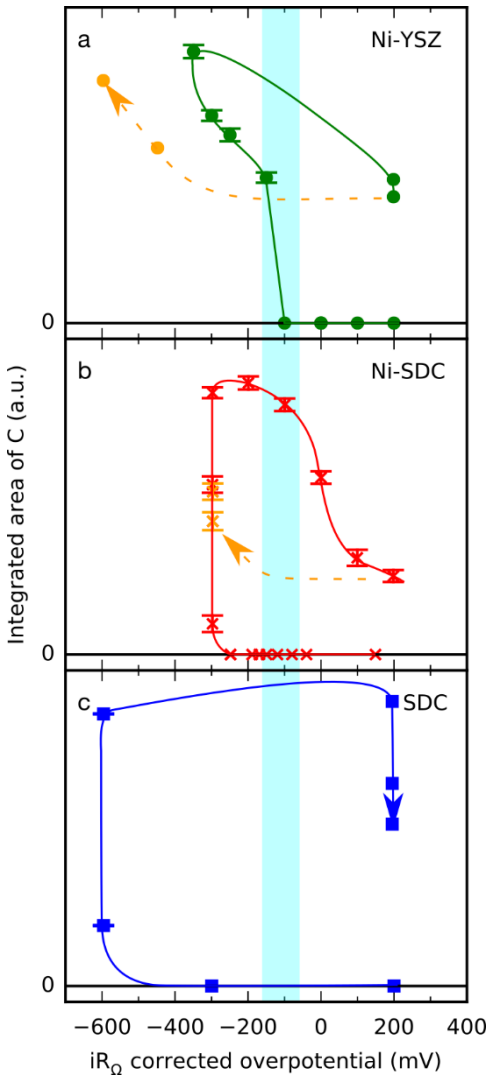

Supplementary Fig. 3.

Partial reversibility of the integrated area of C-C (~285 eV) peaks against overpotential for all three samples.

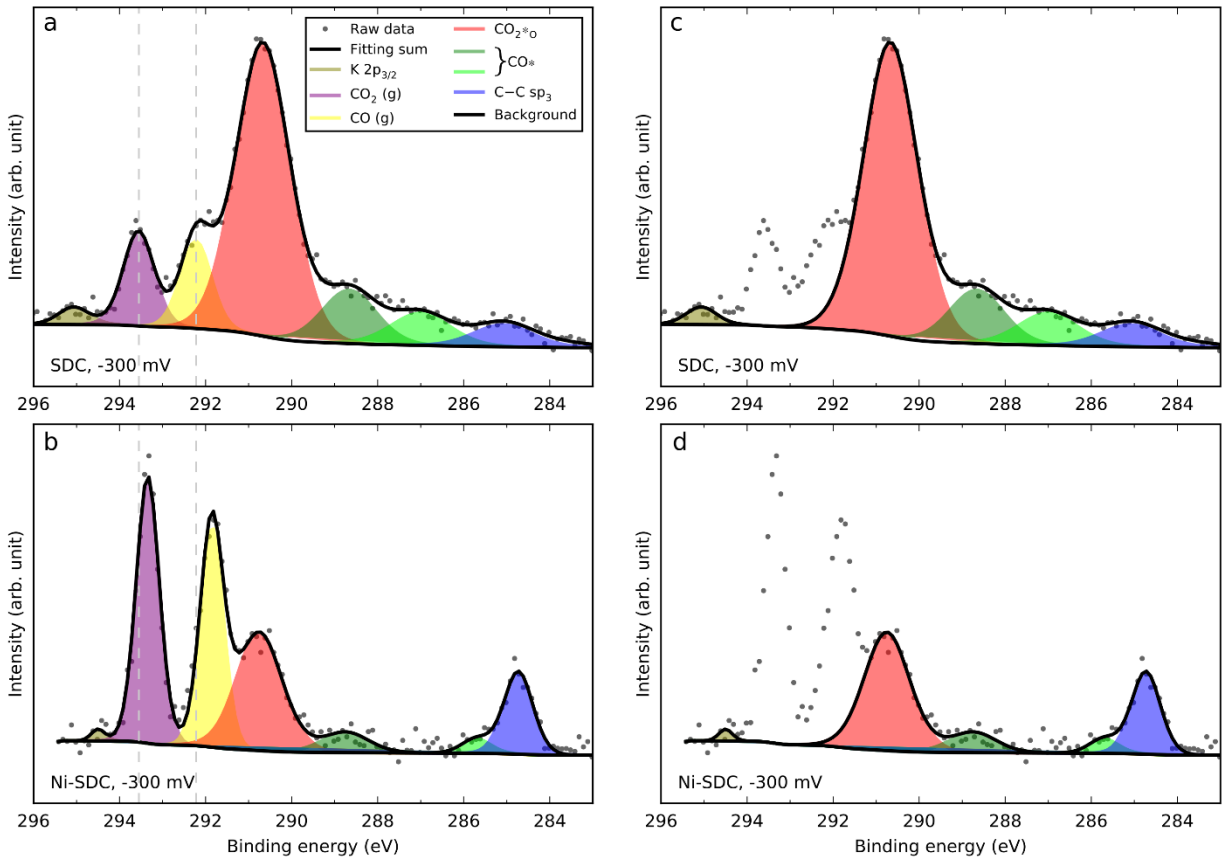

Supplementary Fig. 4.

Removal of gas phase peaks from NAPXPS spectra at −300 mV overpotential. Illustration of all peaks fitted to the raw data and the resulting fitting sum, including the background, for SDC, **a**, and Ni-SDC, **b**. Subsequently, the CO(g) and CO_2(g) peaks are removed for SDC, **c**, and Ni-SDC, **d**.

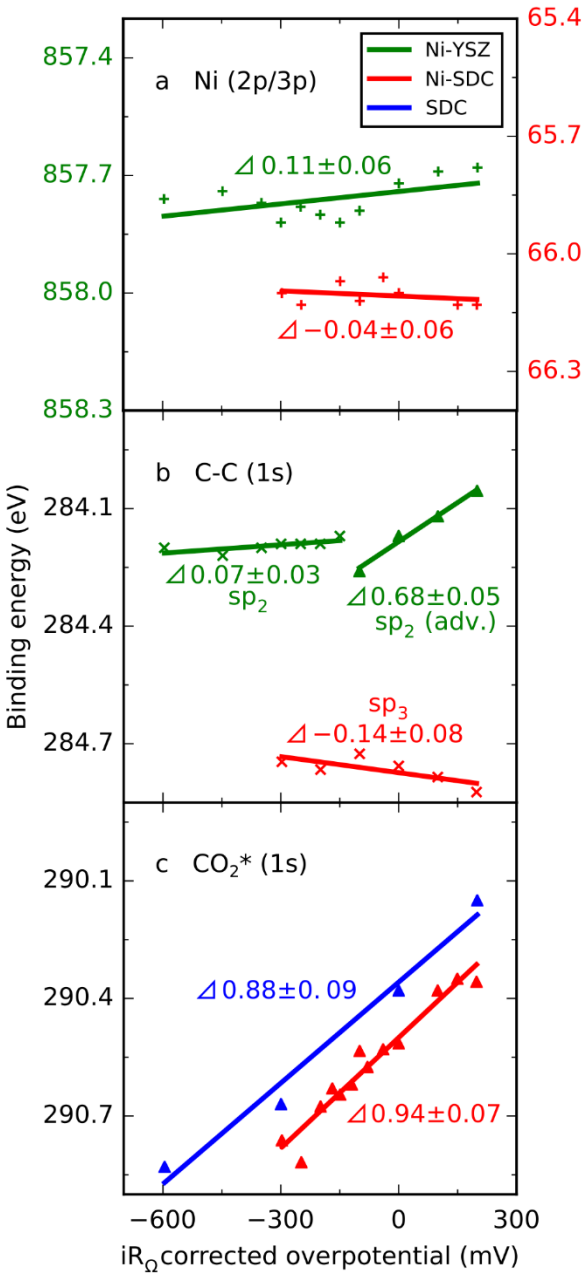

Supplementary Fig. 5.

Shifts of photoemission core-level peaks for different surface species. **a**, Ni 2p for Ni-YSZ and Ni 3p for Ni-SDC. **b**, Carbon peak at ~285 eV, with a sp^2-hybridization carbon peak from adventitious carbon on YSZ and a peak for electrochemically deposited sp^2 carbon on or near nickel on Ni-YSZ, and a deposited carbon peak for Ni-SDC ascribed to sp^3-hybridization. There were insufficient data points to plot the shifting of the carbon peak for the SDC electrode. **c**, Carbonate shifting rigidly with the SDC surfaces. No carbonate peak was identified for the Ni-YSZ electrode. The binding energy of each spectrum at OCV are calibrated with the Au $4f_{7/2}$ peak (84.0 eV) from an Au foil Fermi coupled with the photoelectron analyzer.

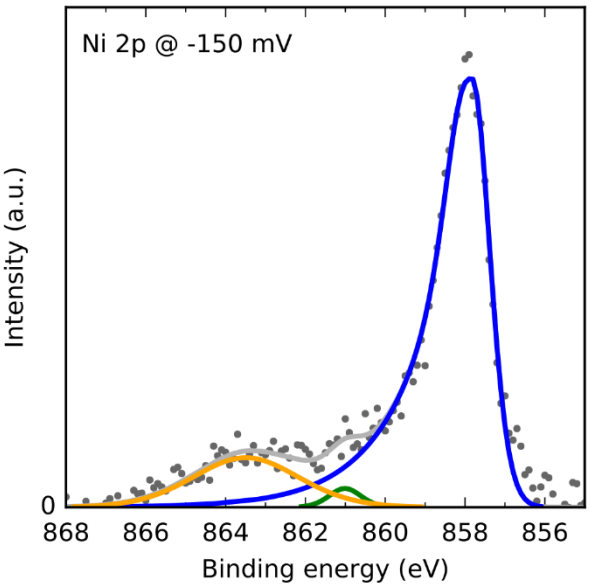

Supplementary Fig. 6.
Ni 2p NAPXPS spectrum measured at -150 mV on the Ni-YSZ electrode. Note: For this spectrum, calibration to Au has not been done, so the exact BE is not correct.

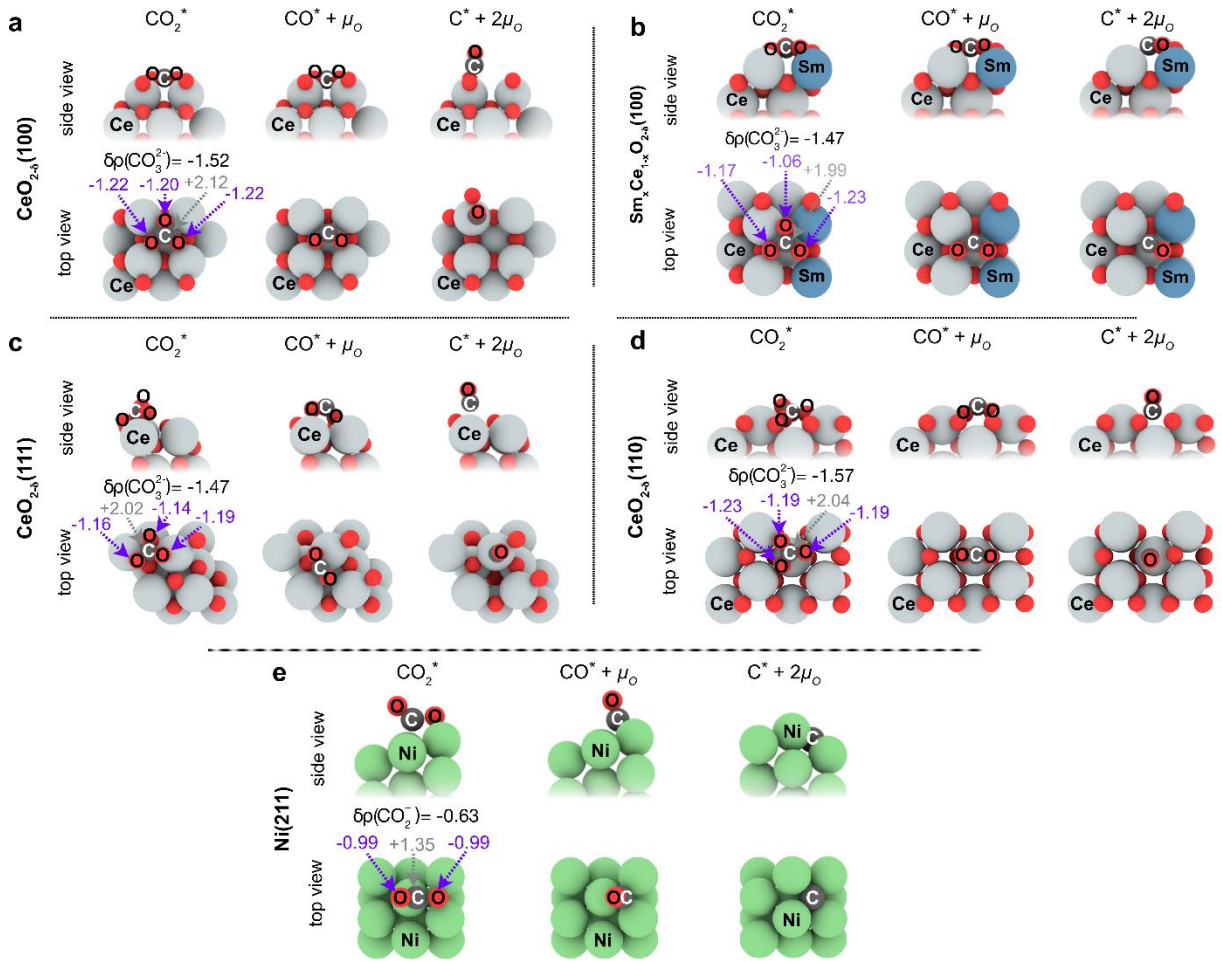

Supplementary Fig. 7.

Calculated geometries and Bader charges associated with CO_2*$_O$/CO_2*. The overall charge of the CO_3/CO_2 is also indicated as δρ. **a-d** Adsorbate charge analysis shows that charge of CO_2*$_O$ is in a narrow range between –1.57 e^- to –1.47 e^- for all surfaces with oxygen vacancy sites supporting the presence of the carbonate species. For (100) surfaces CO_2*$_O$ has a tridentate binding geometry **ab**, for (110) surface a bidentate binding geometry **d**, and for (111) surface a monodentate binding geometry **c** is observed as the most stable. **e** For Ni(211), the bent CO_2 geometry and negative charge of –0.63 e^- is observed. For CO*, the C-O bond lengths analysis indicates that they are 1.295/1.304 Å for $Sm_{0.25}Ce_{1.75}O_{1.875}$(100)/$CeO_{1.875}$(100), 1.255 Å for $CeO_{1.875}$(110) and 1.241 Å for $CeO_{1.875}$(111), and very short 1.194 Å for Ni(211) indicative of single (~1.43 Å) to double (1.20 Å) C–O bond transition.

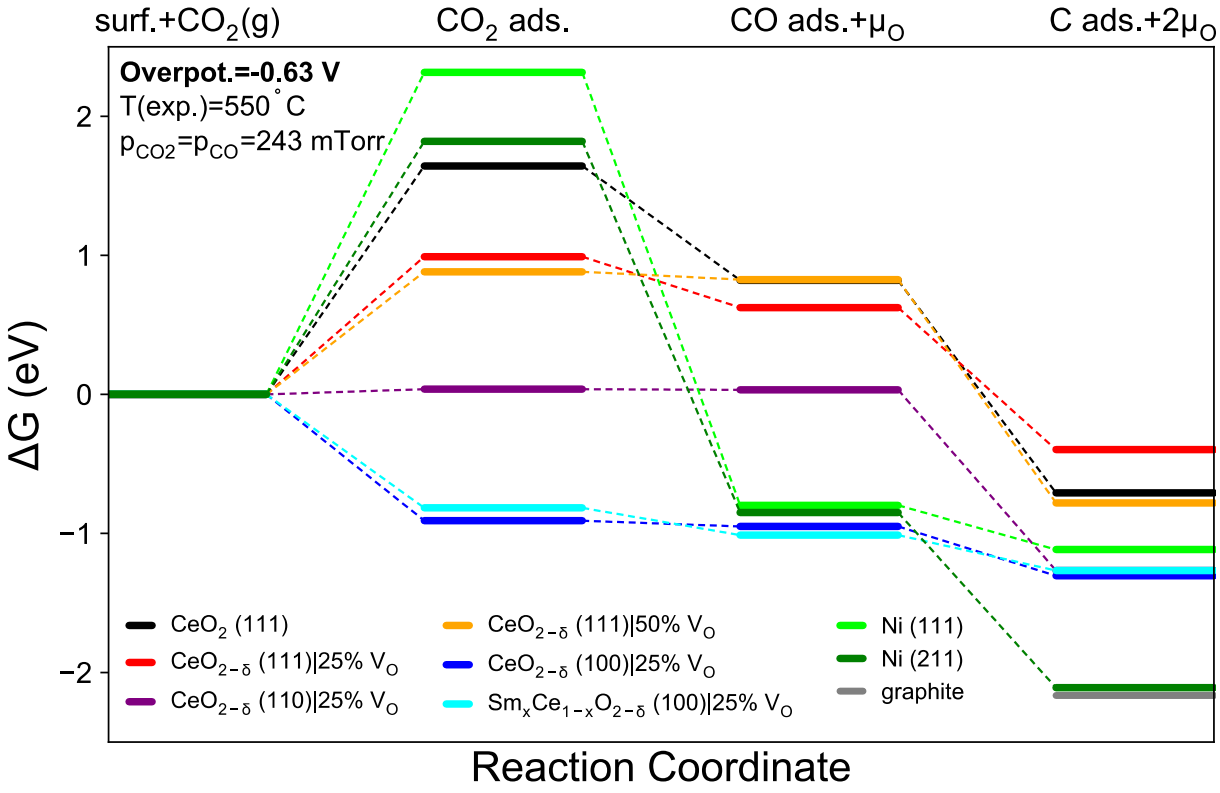

838

839 **Supplementary Fig. 8.**

840 **Calculated free energy along reaction pathway from CO_2* to CO* to C* at the limiting potential of -630**
841 **mV.** At this potential, the last step is the lowest for $CeO_{2-\delta}$ (110) surface.

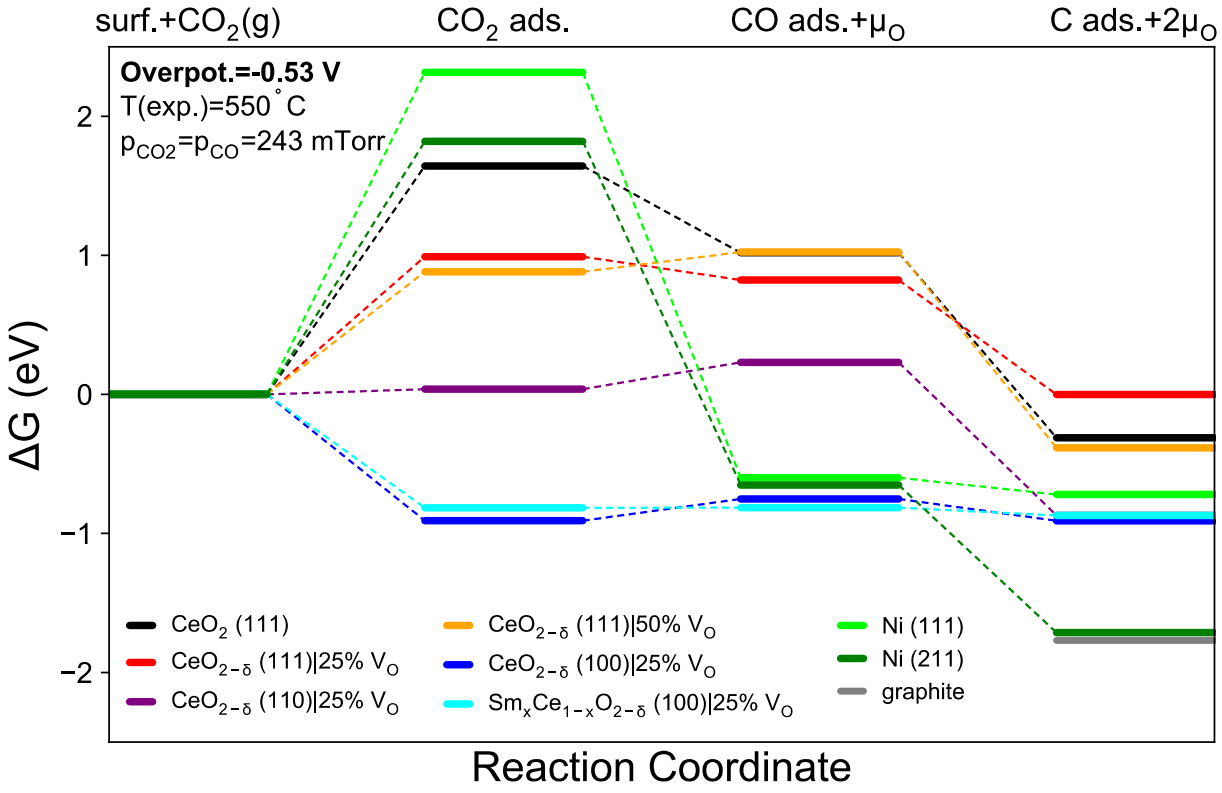

Supplementary Fig. 9.

Calculated free energy along reaction pathway from CO_2* to CO* to C* at the limiting potential of -530 mV. At this potential, the last step is the lowest for $CeO_{2-\delta}$ (111) surface with 25% oxygen vacancy concentration.

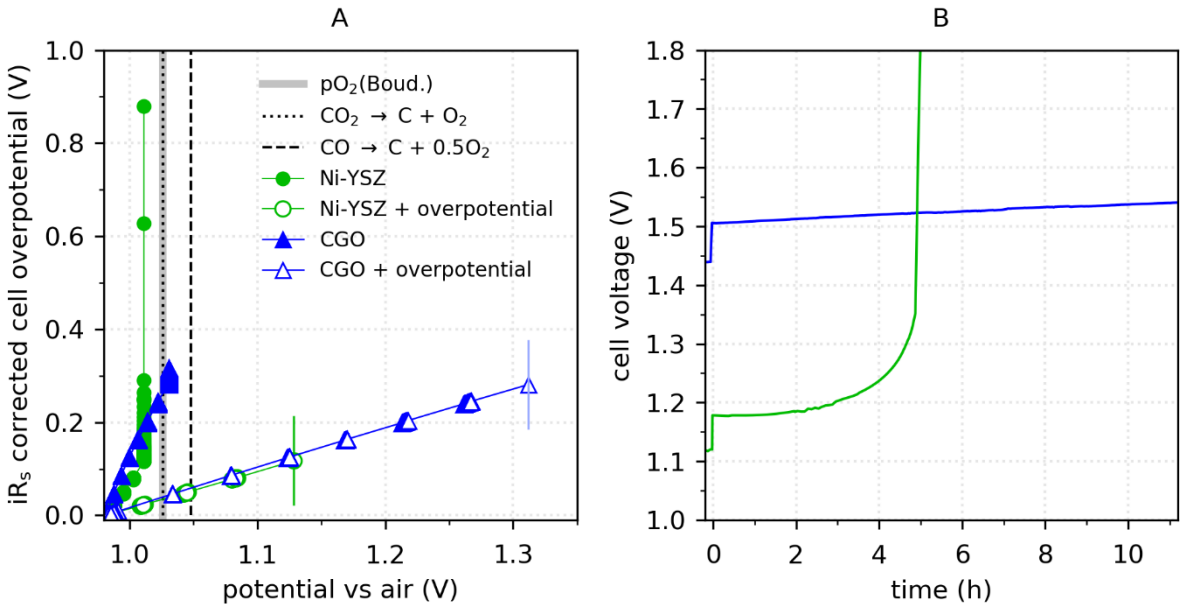

Supplementary Fig. 10.

Comparison of the abilities of scaled-up solid oxide cells with Ni-YSZ vs ceria electrodes to operate in thermodynamic carbon deposition regimes during CO_2 electrolysis. This is another view of the same data shown in Fig. 5. (A) Cell overpotential corrected for ohmic potential drop (iR_S, where R_S is the ohmic area-specific resistance) measured at increasing current densities. The solid symbols are the same data as shown in Fig. 5a, with x-axis now as potential vs air of the outlet CO/CO_2 gas. The thick light-gray vertical line labeled pO_2(Boud.) is the carbon deposition threshold for the Boudouard reaction, the threshold that is relevant for the solid symbols. For the x-axis values of the open symbols, the iR_S corrected cell overpotential has been added to the gas phase chemical potential (pO_2). This includes both the fuel-electrode and oxygen-electrode overpotentials – ideally only the fuel-electrode overpotential would be added by quantifying individually using detailed impedance analysis, but we did not have a sufficient set of impedance measurements to do so, and the oxygen-electrode overpotential is much smaller than the fuel-electrode overpotential in both of these cells, so these values serve as a rough approximation. Therefore, the more precisely quantified outlet pCO values are shown in Fig. 5 rather than these approximate values. The points at which degradation sets in (visible in the solid symbols at the same y-values) are marked with short vertical lines. The two dashed vertical lines are the thermodynamic thresholds for the electrochemical carbon deposition reactions, the thresholds that are relevant for the open symbols. (B) Cell voltages measured at fixed current densities at the final operating points shown in (A). This is the same data as in Fig. 5b, but with the cell voltage on the y-axis rather than the iR_S corrected cell overpotential. The main reason for the much higher cell operating voltage (before Ni-YSZ degradation) for the ceria-electrode cell is the much higher ohmic resistance of the thick electrolyte in this electrolyte-supported cell (the electrolyte in the Ni-YSZ-supported cell is more than 10x thinner).

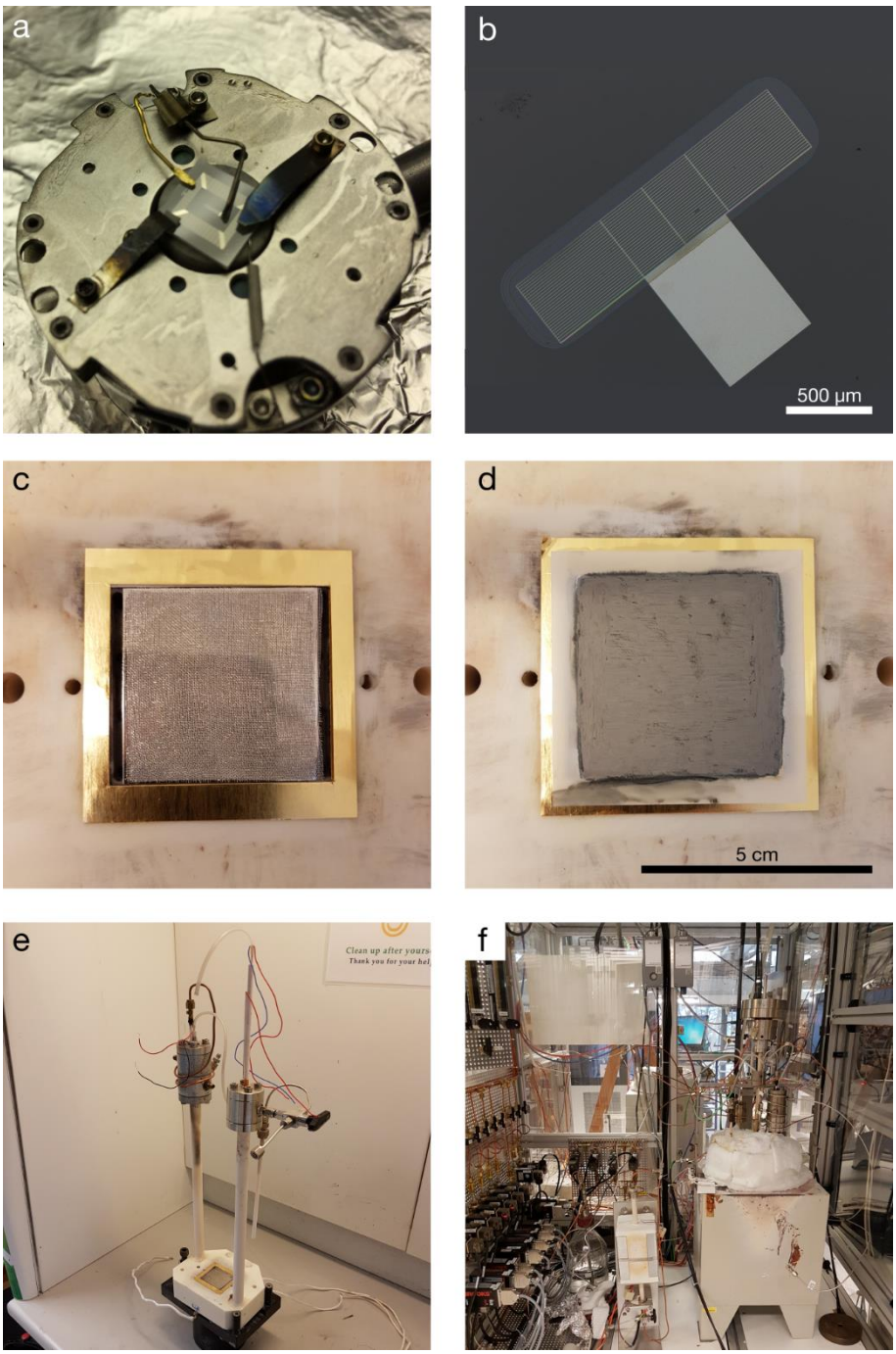

Supplementary Fig. 11.

Experimental setups for APXPS and large-scale cell testing. **a**, Sample holder and sample for the APXPS experiments, and **b**, an optical microscope image of one of the samples. **c-f**, Mounting the large-scale cell in a test rig. The Pt contacting mesh and Au sealing are placed (**c**), followed by the cell (**d**), in the cell testing "house" (**e**), which is subsequently lowered into the furnace (**f**), surrounded by gas tubing and electrical wiring.

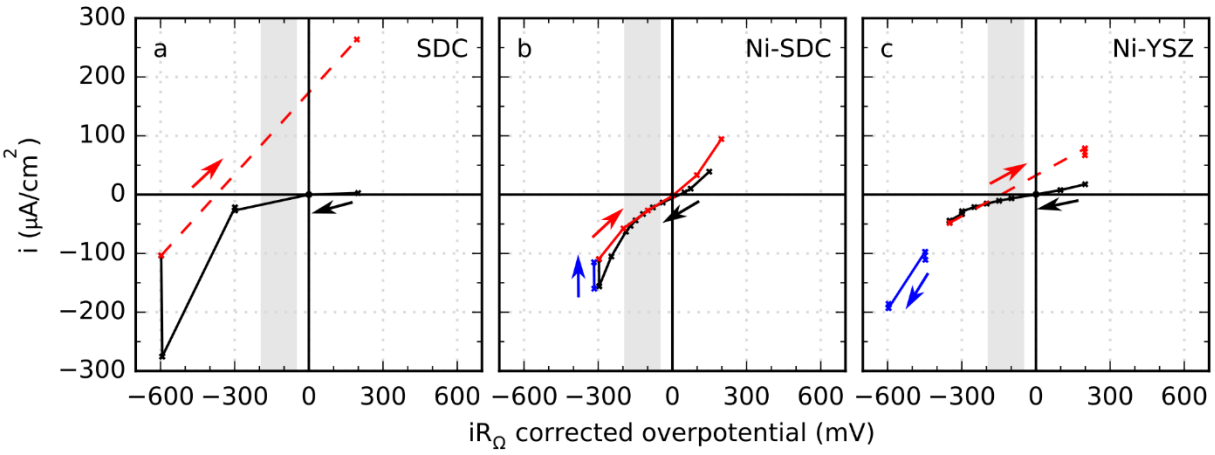

Supplementary Fig. 12.

iV plots with hysteresis for the three samples. a, SDC, b, Ni-SDC and c, Ni-YSZ. The fixed potential was corrected for the Ohmic resistance of the YSZ electrolyte. The arrows indicate the chronological order in which measurements were recorded, with black first, red second and blue third. The thermodynamic threshold for carbon formation is shown by the gray box, accounting for experimental uncertainties and differences.

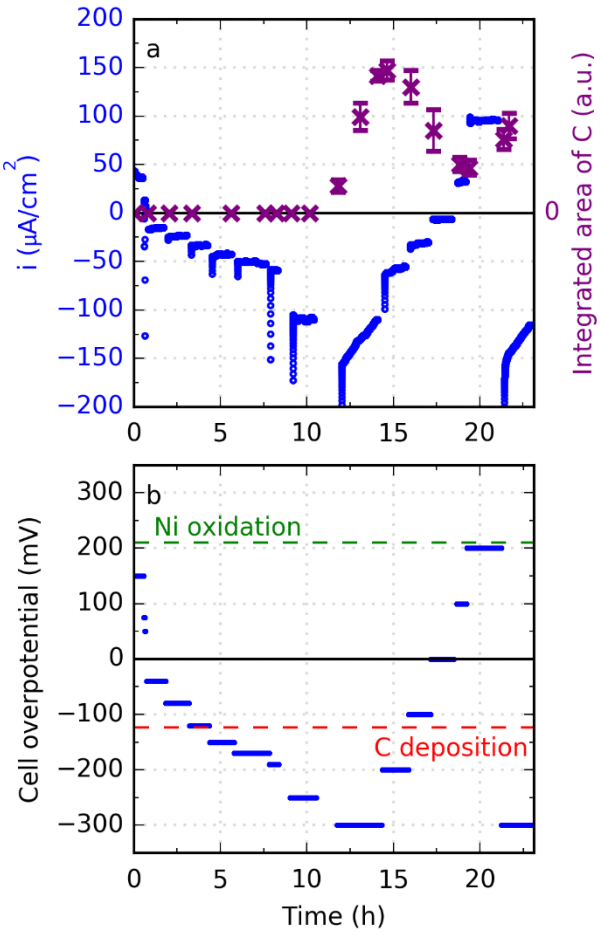

Supplementary Fig. 13.

The response of the current and carbon coverage to the changing potential throughout the Ni-SDC experiment. The SDC and Ni-YSZ electrodes have similar, but not identical behavior. **a**, current density and the integrated area of the C peak changing with time. **b**, the applied voltage changing with time. The upper limit of Ni oxidation is also plotted (--), and the carbon deposition threshold (--) which was intentionally crossed. After 12 h, when -300 mV is applied, the current drops considerably and carbon coverage increases. When decreasing the cathodic potential below the thermodynamic threshold for carbon formation, the carbon coverage decreases and the current stabilizes. The results were reproduced at the end of the experiment by applying -300 mV again.

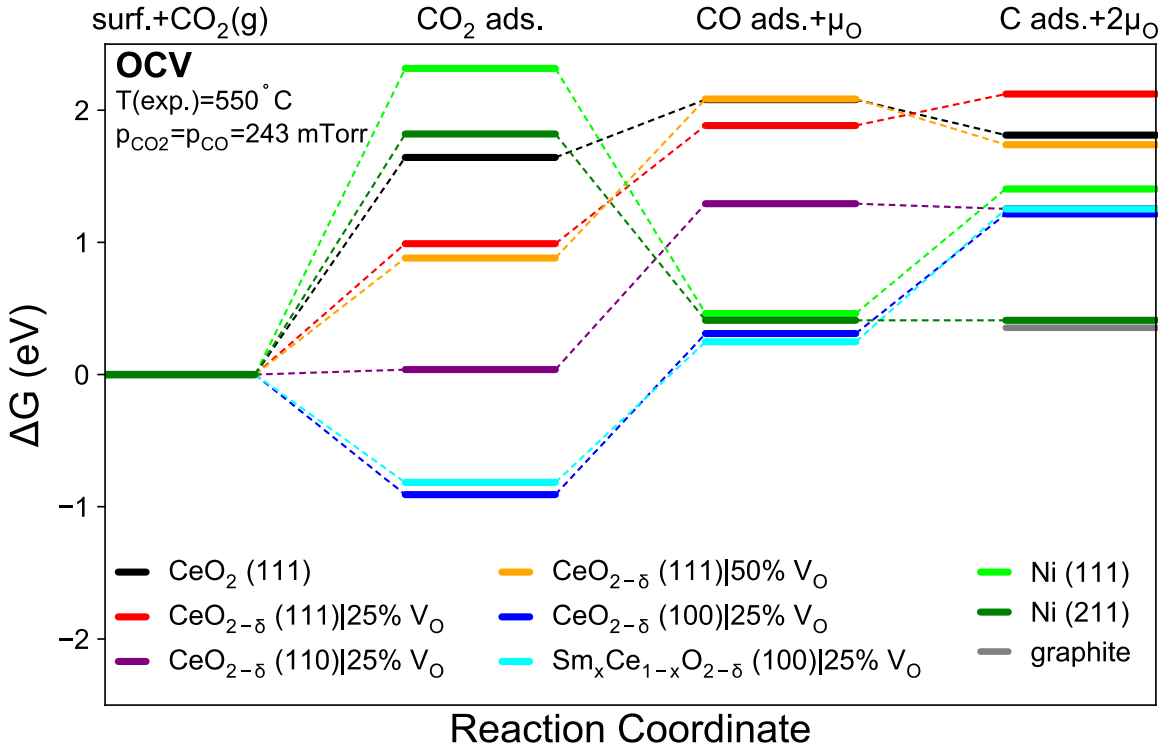

Supplementary Fig. 14.

Calculated free energy along reaction pathway from CO_2* to CO* to C* at OCV for all considered surfaces. Increasing vacancy concentration for ceria (111) surfaces from 0% to 25% to 50% clearly stabilizes CO_2 adsorption and destabilizes C adsorption. CO-like species is formed for C* adsorption for all ceria surfaces. For completeness, we also compare the (100) surfaces of $Sm_xCe_{1-x}O_{2-\delta}$ to $CeO_{2-\delta}$.

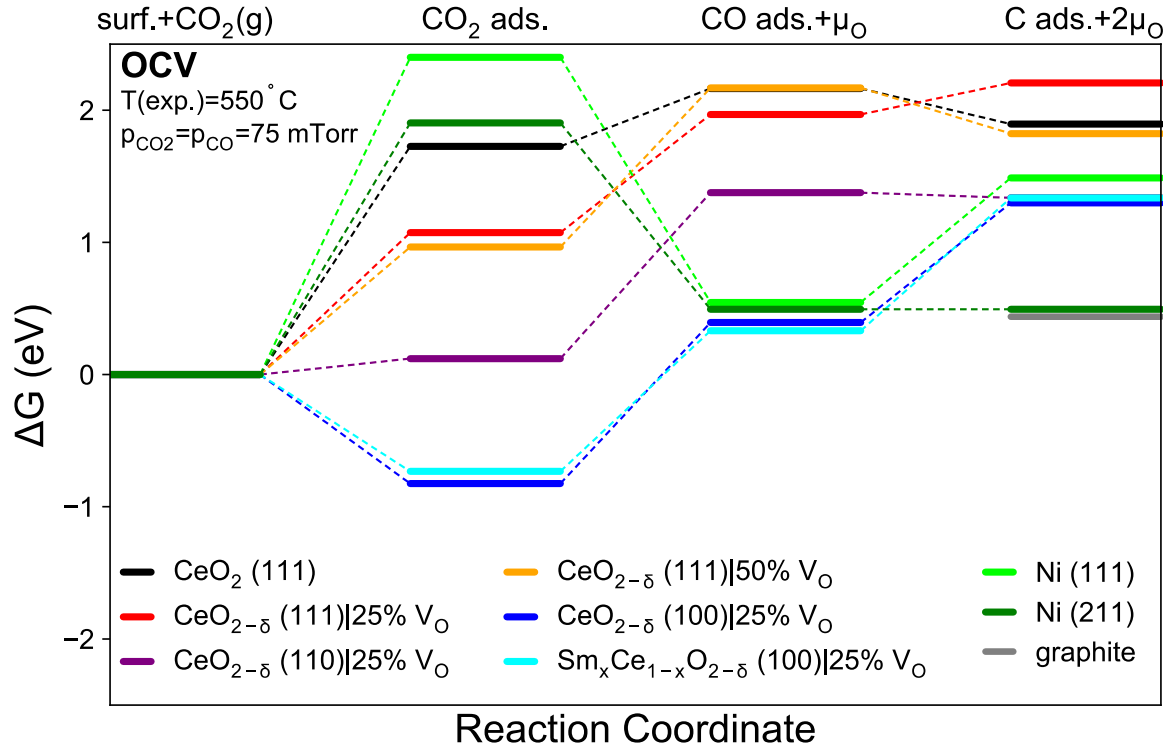

904

905 **Supplementary Fig. 15.**

906 **Calculated free energy along reaction pathway from CO_2* to CO* to C* at OCV for all**
907 **considered surfaces at a reduced total CO/CO_2 pressure of 150 mTorr.**

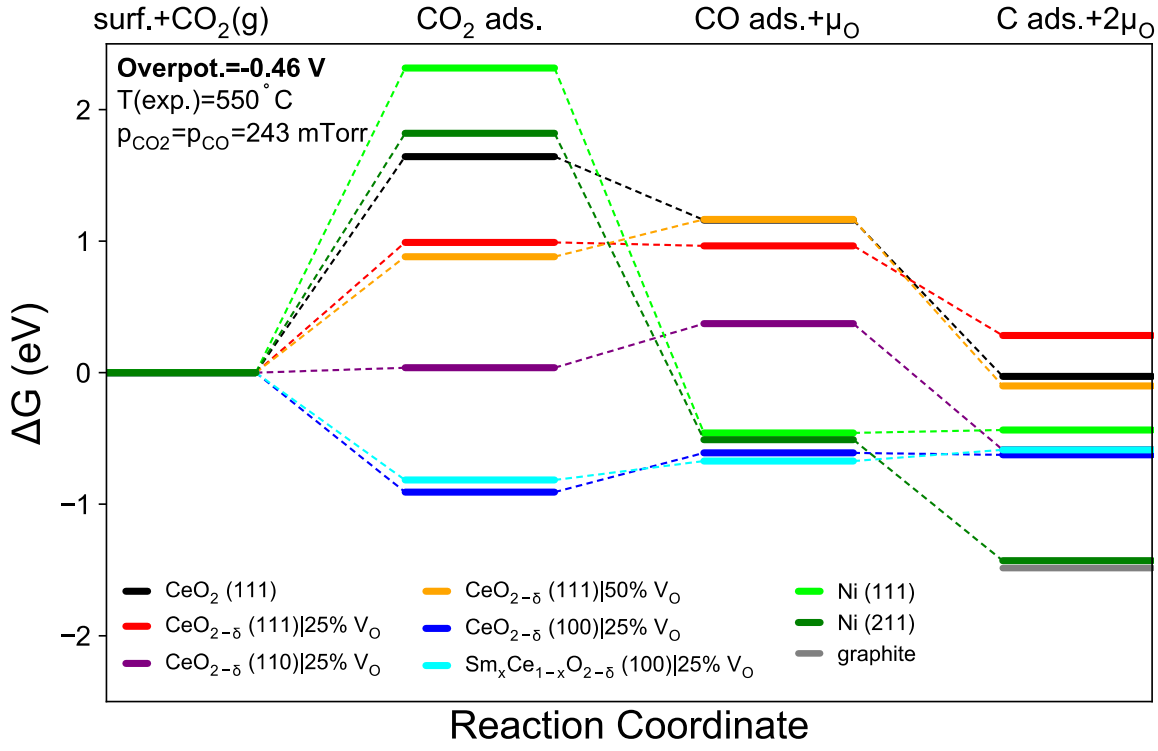

Supplementary Fig. 16.

Calculated free energy along reaction pathway from CO_2* to CO* to C* at the limiting potential of -460 mV. At this potential, the last step is the lowest for CeO_2 (111) surface without oxygen vacancies.

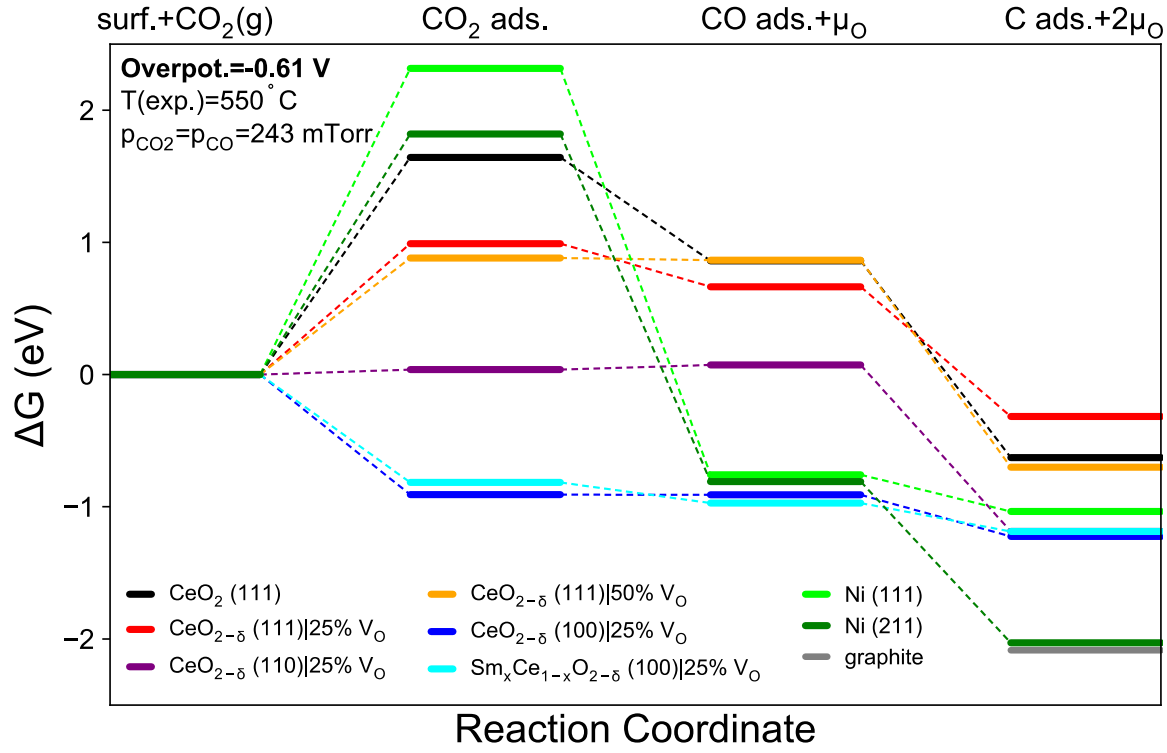

Supplementary Fig. 17.

Calculated free energy along pathway from CO_2* to CO* to C* at the limiting potential of -610 mV. At this potential, the is the lowest for $CeO_{2-\delta}$ (111) surface with 50% oxygen vacancy concentration.

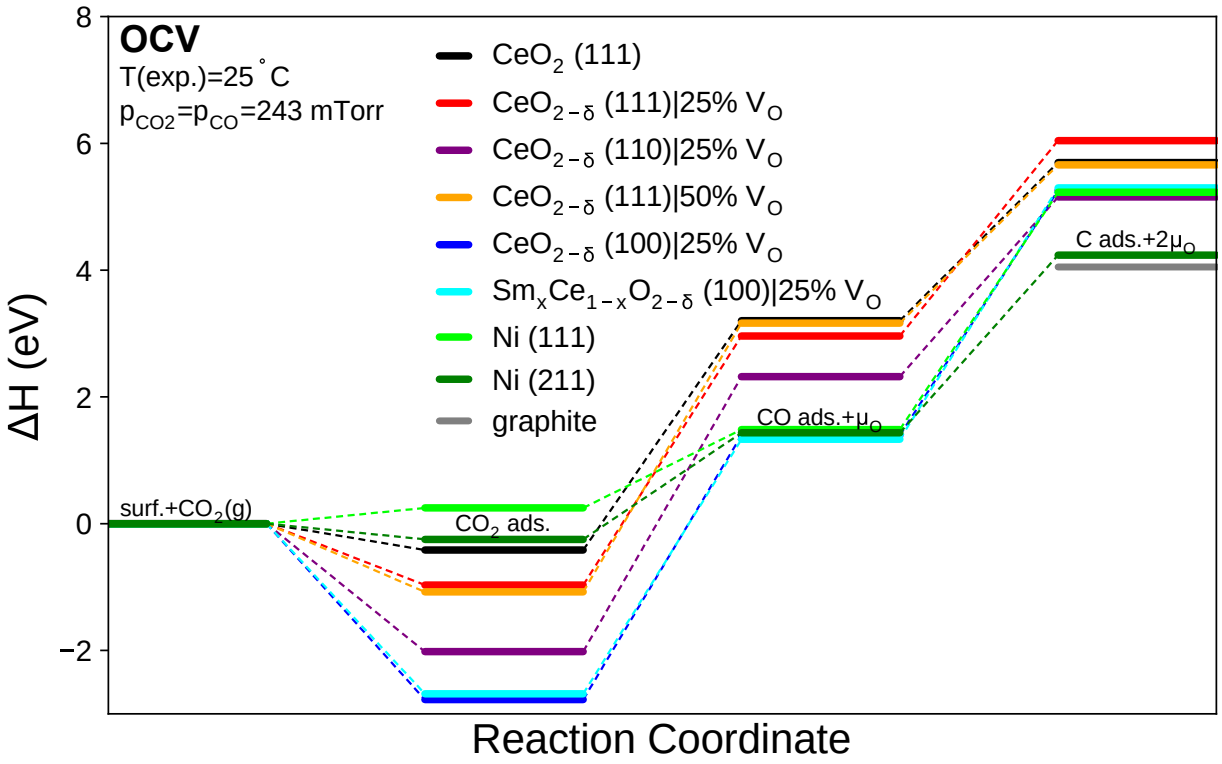

Supplementary Fig. 18.

Calculated enthalpy along the reaction pathway from CO_2* to CO* to C* at OCV for all considered surfaces.

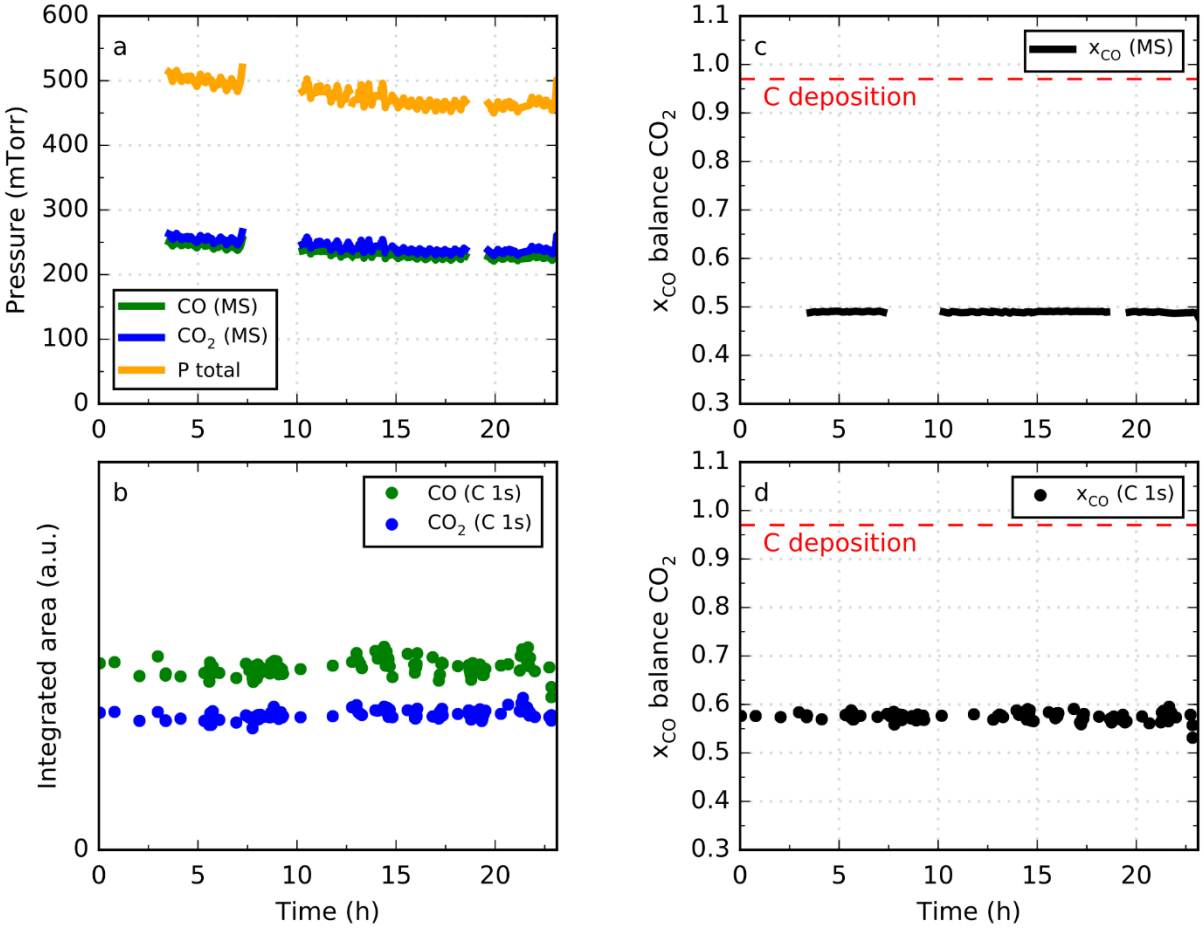

Supplementary Fig. 19.

Pressure and gas composition throughout the Ni-SDC experiment measured using mass-spectroscopy and the XPS C 1s spectra. **a**, total, CO and CO_2 pressure in mTorr measured by a mass-spectrometer (MS). The data has been smoothed slightly to remove excessive noise in pressure measurements while moving the sample stage. **b**, integrated area of the CO and CO_2 peaks from C 1s after calibrating for the difference in electron-molecule scattering cross-sections ($1.449 \cdot 10^{-20}$ m^2 and $2.177 \cdot 10^{-20}$ m^2 at 490 eV, respectively). **c**, the CO:CO_2-ratio from the mass-spectrometer and the carbon deposition threshold. **d**, the CO:CO_2-ratio from C 1s peaks and the carbon deposition threshold. The CO:CO_2-ratio agrees fairly well between the two measuring techniques, although the result from XPS is about 7-8% x_{CO} higher.

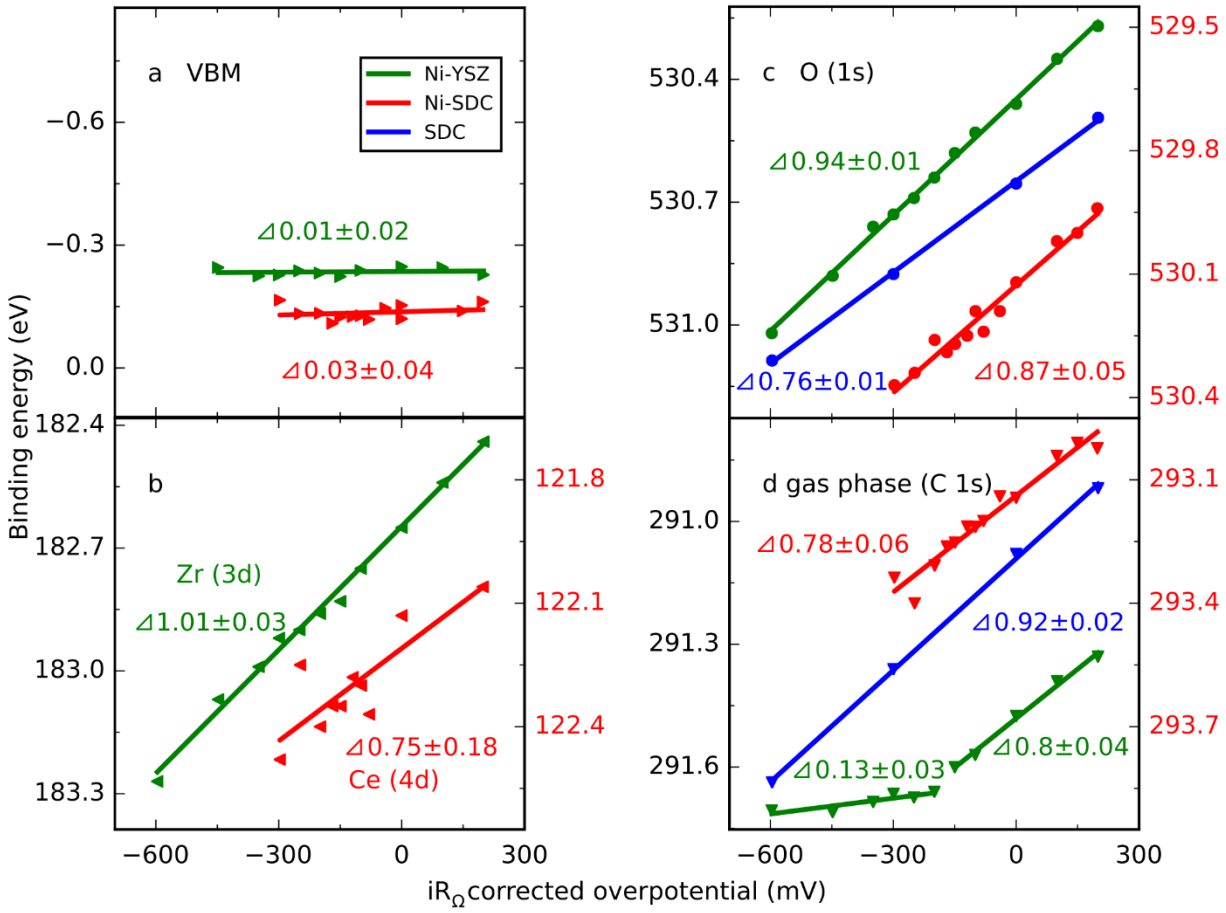

Supplementary Fig. 20.

Shifts of XPS core-level peaks for different surface species. **a**, Valence band maximum (VBM) dominated by Ni. A small systematic shift from the expected value of 0 eV is likely related to the quantification method. **b**, Zr 3d for Ni-YSZ and Ce 4d for Ni-SDC. **c**, lattice oxygen. **d**, CO_2 gas phase for SDC and Ni-SDC, and CO gas phase for Ni-YSZ. The changing slope observed for gas phase on Ni-YSZ was confirmed by the shifts of CO- and CO_2-gas phase core-level peaks from the O 1s spectrum, and correlates with the suggested onset of -150 mV shown in Fig. 1g and Supplementary Fig. 5.

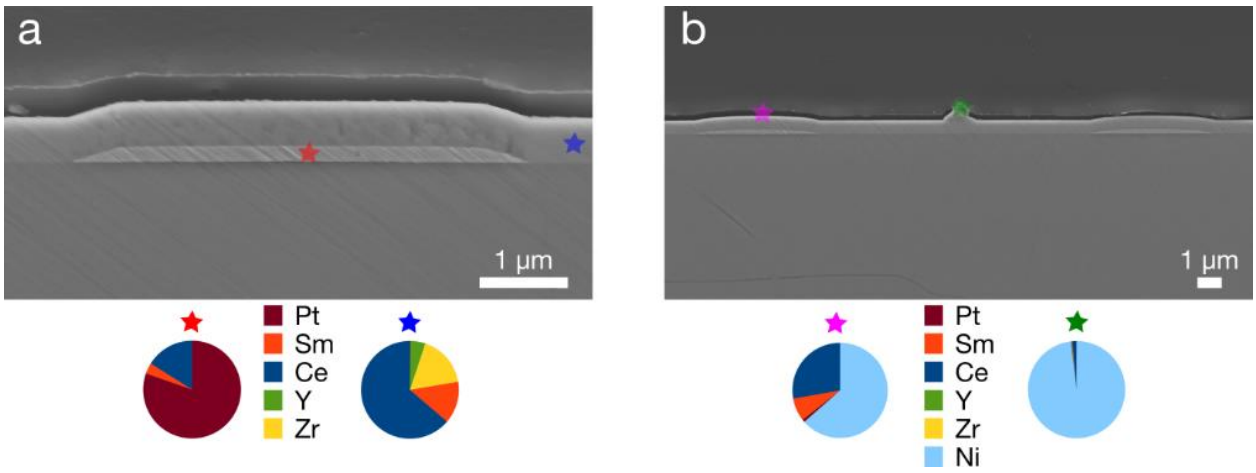

Supplementary Fig. 21.

Scanning electron microscopy images of cross sections and chemical composition of the samples. **a**, A Pt wire buried by a SDC layer for the SDC sample. **b**, Two Pt wires buried by a SDC layer, with Ni nanoparticles of varying size on the surface, for the Ni-SDC sample. Elemental composition was determined by energy-dispersive x-ray spectroscopy in the scanning electron microscope.

Supplementary Table 1.

Peak assignment for C 1s at OCV.

Specie	Approx. BE (eV)	BE constraints (eV)	FWHM (eV)	FWHM constraints (eV)	Ref.
CO_2 (gas)	293.0-293.3	293.0-294.5	0.6	<1.1	[6,10,11]
CO (gas)	291.5-291.9	290.0-293.0	0.6	= FWHM(CO_2(gas))	[12]
CO_2*	290.4-290.6		1.35	<1.55	[6,10,11,13–15]
CO*	288.0-289.0	287.0-289.0	1.35	= FWHM (CO_2*)	[13,15–18]
CO*	287.4-287.6	286.0-288.0	1.35	= FWHM (CO_2*)	[13,15–18]
CO*	285.5-286.0	285.5-286.0	1.4-1.55	= FWHM (CO_2*)	[13,15–18]
C-C sp^3	284.8	284.7-284.9	0.7	0.7	[2,4,18–22]
C-C sp^2 (adv.)	284.3*	284.1-284.3*	1.3	1.3	[2,4,18–21]
C-C sp^2	284.3	284.1-284.3	1.3	1.3	[2,4,18–22]

* Before electrochemical carbon deposition. After deposition, the BE was strictly constrained to continue the linear BE shift with applied potential as observed prior to deposition (see Supplementary Fig. 5b).

Supplementary Table 2.

Peak assignment for O 1s at OCV.

Specie	Approx. BE (eV)	BE constraints (eV)	FWHM (eV)	FWHM constraints (eV)	Ref.
CO (gas)	538.1		1.0	= FWHM (CO_2(gas))	[12]
CO_2 (gas)	536.9		1.0		[6,10,11]
C adsorbates	532.5-532.7		1.5	= FWHM (Lattice O)	[6,10,11,22]
Si impurities	531.3-531-5		1.5	= FWHM (Lattice O)	[6,23]
Lattice O	529.9-530.1		1.5		[6,10,11,23]

Supplementary Table 3.

Complete list of DFT calculated limiting potentials for reduction of CO_2(g) to C for considered surfaces. For nickel surfaces, the reaction processes directly from CO(g) as opposed to CO_2(g) due to highly unfavorable CO_2* energy.

	Calculated η (mV)	[V_O] (%)	Potential limiting step
Ni(211)	-110	0	CO* → C*
Ni(111)	-460	0	CO* → C*
CeO_2(111)	-460	0	CO*o → C*o
CeO_{2-x}(111)	-530	25	CO*o → C*o
$Sm_xCe_{1-x}O_{2-\delta}$ (100)	-530	25	CO_2*o → CO*$_O$
$CeO_{2-\delta}$ (100)	-610	25	CO_2*o → CO*$_O$
$CeO_{2-\delta}$ (111)	-610	50	CO_2*o → CO*$_O$
$CeO_{2-\delta}$ (110)	-630	25	CO_2*o → CO*$_O$

Supplementary Table 4.

Calculated adsorption energies (ΔE) and Gibbs energies (ΔG, at OCV relative to μO) of CO_2*, CO* and C* used for construction of Gibbs energy diagrams (Fig. 4, Supplementary Fig. 8-9 and Supplementary Fig. 14-17). The associated structures are also available online [24]. To construct the ΔGs from ΔEs, we have corrected O_2(g) DFT-PBE reference energy by +0.38 eV to match the experimental enthalpy of $\Delta H(H_2(g)+1.2O_2(g)\rightarrow H_2O(g))$ and used the Gibbs energy corrections in Supplementary Table 5.

Surface	$CO_2(g)+*\rightarrow CO_2*$		$CO_2(g)-0.5O_2(g)+*\rightarrow CO*$		$CO_2(g)-O_2(g)+*\rightarrow C*$	
	ΔE[eV]	ΔG[eV]	ΔE[eV]	ΔG[eV]	ΔE[eV]	ΔG[eV]
Ni(111)	0.32	2.32	1.35	0.46	4.95	1.40
Ni(211)	-0.16	1.82	1.30	0.41	3.95	0.41
CeO_2(111)	-0.46	1.64	3.05	2.08	5.42	1.81
$CeO_{2-\delta}$(111)|25%V_O	-1.01	0.99	2.79	1.88	5.78	2.12
$CeO_{2-\delta}$(111)|50%V_O	-1.11	0.88	2.99	2.09	5.39	1.74
$CeO_{2-\delta}$(110)|25%V_O	-2.07	0.04	2.14	1.29	4.86	1.25
$CeO_{2-\delta}$(100)|25%V_O	-2.84	-0.91	1.22	0.31	4.96	1.22
$Sm_xCe_{1-x}O_{2-\delta}$(100)|25%V_O	-2.75	-0.82	1.34	0.25	5.38	1.25

974 **Supplementary Table 5.**

975 Table of thermodynamic corrections for gas-phase molecular species as well as the adsorbates in eV
976 at OCV.

molecular species	E_{ZPE}	C_v	ΔH	-TS	ΔG
$O_2(g)$	0.098	0.261	0.359	-6.436	-6.076
$CO_2(g)$	0.311	0.346	0.657	-2.858	-2.202
$CO(g)$	0.135	0.254	0.389	-2.546	-2.157
$CO_3@CeO_2(111)$	0.441	0.522	0.963	-1.126	-0.163
$CO_2@CeO_2(111)$	0.192	0.305	0.497	-0.766	-0.269
$CO@CeO_2(111)$	0.146	0.198	0.345	-0.563	-0.218
$O@CeO_2(111)$	0.054	0.163	0.217	-0.360	-0.143
$CO_3@CeO_{2-x}(111)$	0.434	0.529	0.963	-1.194	-0.231
$CO_2@CeO_{2-x}(111)$	0.293	0.426	0.720	-1.022	-0.303
$CO@CeO_{2-x}(111)$	0.142	0.200	0.342	-0.567	-0.225
$O@CeO_{2-x}(111)$	0.065	0.155	0.219	-0.324	-0.105
$CO_2@Ni(211)$	0.257	0.311	0.568	-0.710	-0.142
$CO@Ni(211)$	0.191	0.291	0.482	-0.666	-0.184
$C@Ni(211)$	0.104	0.127	0.231	-0.239	-0.008
$CO_3@CeO_{2-x}(100)$	0.444	0.522	0.967	-1.175	-0.208
$CO_2@CeO_{2-x}(100)$	0.289	0.417	0.706	-0.926	-0.220
$CO@CeO_{2-x}(100)$	0.147	0.253	0.400	-0.631	-0.231
$O@CeO_{2-x}(100)$	0.060	0.090	0.150	-0.170	-0.020
$CO_3@CeO_{2-x}(110)$	0.446	0.518	0.965	-1.132	-0.167
$CO_2@CeO_{2-x}(110)$	0.297	0.424	0.721	-1.011	-0.290
$CO@CeO_{2-x}(110)$	0.160	0.248	0.409	-0.628	-0.219
$O@CeO_{2-x}(110)$	0.054	0.163	0.218	-0.366	-0.149

977
978

References for Supporting Information:

1. Bale, C. W. *et al.* FactSage thermochemical software and databases - recent developments. *CALPHAD* **33,** 295–311 (2009).
2. Haerle, R., Riedo, E., Pasquarello, A. & Baldereschi, A. sp2/sp3 hybridization ratio in amorphous carbon from C 1s core-level shifts: X-ray photoelectron spectroscopy and first-principles calculation. *Phys. Rev. B* **65,** 045101 (2001).
3. Doniach, S. & Sunjic, M. Many-electron singularity in X-ray photoemission and X-ray line spectra from metals. *J. Phys. C Solid State Phys.* **3,** 285–291 (1970).
4. Chen, C. T. & Sette, F. High Resolution Soft X-Ray Spectroscopies with the Dragon Beamline. *Phys. Scr.* **T31,** 119–126 (1990).
5. Díaz, J., Paolicelli, G., Ferrer, S. & Comin, F. Separation of the sp3 and sp2 in the C1s photoemission spectra of amorphous carbon film. *Phys. Rev. B* **54,** 8064–8069 (1996).
6. Feng, Z. a., Machala, M. L. & Chueh, W. C. Surface electrochemistry of CO2 reduction and CO oxidation on Sm-doped CeO2-x: coupling between Ce3+ and carbonate adsorbates. *Phys. Chem. Chem. Phys.* **17,** 12273–12281 (2015).
7. Opitz, A. K. *et al.* Surface Chemistry of Perovskite-Type Electrodes During High Temperature CO 2 Electrolysis Investigated by Operando Photoelectron Spectroscopy. *ACS Appl. Mater. Interfaces* **9,** 35847–35860 (2017).
8. Skafte, T. L., Graves, C., Blennow, P. & Hjelm, J. Carbon Deposition during CO2 Electrolysis in Ni-Based Solid-Oxide-Cell Electrodes. *ECS Trans.* **68,** 3429–3437 (2015).
9. Graves, C., Chatzichristodoulou, C. & Mogensen, M. Kinetics of CO/CO2 and H2/H2O reactions at Ni-based and ceria-based solid-oxide-cell electrodes. *Faraday Discuss.* **182,** 75–95 (2015).
10. Yu, Y. *et al.* CO 2 activation and carbonate intermediates: an operando AP-XPS study of CO 2 electrolysis reactions on solid oxide electrochemical cells. *Phys. Chem. Chem. Phys.* **16,** 11633–11639 (2014).
11. Deng, X. *et al.* Surface Chemistry of Cu in the Presence of CO 2 and H 2 O. *Langmuir* **24,** 9474–9478 (2008).
12. Norton, P. R. & Tapping, R. L. Photoelectron spectroscopy studies of the adsorption of CO and CO2 on nickel, platinum and copper. *Chem. Phys. Lett.* **38,** 207–212 (1976).
13. Mudiyanselage, K. *et al.* Importance of the Metal-Oxide Interface in Catalysis: In Situ Studies of the Water-Gas Shift Reaction by Ambient-Pressure X-ray Photoelectron Spectroscopy. *Angew. Chemie - Int. Ed.* **52,** 5101–5105 (2013).
14. Senanayake, S. D. *et al.* Probing the reaction intermediates for the water-gas shift over inverse CeOx/Au(111) catalysts. *J. Catal.* **271,** 392–400 (2010).
15. Staudt, T. *et al.* Electronic Structure of Magnesia-Ceria Model Catalysts, CO2 Adsorption, and CO2 Activation: A Synchrotron Radiation Photoelectron Spectroscopy Study. *J. Phys. Chem. C* **115,** 8716–8724 (2011).
16. Czekaj, I. *et al.* Characterization of surface processes at the Ni-based catalyst during the methanation of biomass-derived synthesis gas: X-ray photoelectron spectroscopy (XPS). *Appl. Catal. A Gen.* **329,** 68–78 (2007).
17. Ming, H. *et al.* Large scale electrochemical synthesis of high quality carbon nanodots and their photocatalytic property. *Dalt. Trans.* **41,** 9526 (2012).
18. Ermolieff, A. *et al.* XPS, Raman spectroscopy, X-ray diffraction, specular X-ray reflectivity, transmission electron microscopy and elastic recoil detection analysis of emissive carbon film characterization. *Surf. Interface Anal.* **31,** 185–190 (2001).
19. Morar, J. F. *et al.* C 1s excitation studies of diamond (111). I. Surface core levels. *Phys. Rev. B* **33,** 1346–1349 (1986).
20. Mizokawa, Y. The C KLL first-derivative x-ray photoelectron spectroscopy spectra as a fingerprint of the carbon state and the characterization of diamondlike carbon films. *J. Vac. Sci. Technol. A Vacuum, Surfaces, Film.* **5,** 2809 (1987).

21. Brühwiler, P. A. *et al.* π* and σ* Excitons in C 1s Absorption of Graphite. *Phys. Rev. Lett.* **74,** 614–617 (1995).
22. Blume, R. *et al.* The influence of intercalated oxygen on the properties of graphene on polycrystalline Cu under various environmental conditions. *Phys. Chem. Chem. Phys.* **16,** 25989–6003 (2014).
23. Feng, Z. a., El Gabaly, F., Ye, X., Shen, Z.-X. & Chueh, W. C. Fast vacancy-mediated oxygen ion incorporation across the ceria-gas electrochemical interface. *Nat. Commun.* **5,** 1–9 (2014).
24. Bajdich, M. https://www.catalysis-hub.org/publications/SkafteOxidized2018. (2018).